TOI-1452 b: SPIRou and TESS Reveal a Super-Earth in a Temperate Orbit Transiting an M4 Dwarf

Charles Cadieux, René Doyon, Mykhaylo Plotnykov, Guillaume Hébrard, Farbod Jahandar, Étienne Artigau, Diana Valencia, Neil J. Cook, Eder Martioli, Thomas Vandal, et al.

CrossMark

TOI-1452 b: SPIRou and TESS Reveal a Super-Earth in a Temperate Orbit Transiting an M4 Dwarf

Charles Cadieux[1] , René Doyon[1,2] , Mykhaylo Plotnykov[3] , Guillaume Hébrard[4] , Farbod Jahandar[1] , Étienne Artigau[1,2] ,
Diana Valencia[5,6] , Neil J. Cook[1] , Eder Martioli[4,7] , Thomas Vandal[1] , Jean-François Donati[8] , Ryan Cloutier[9,42] ,
Norio Narita[10,11,12] , Akihiko Fukui[10,12] , Teruyuki Hirano[11,13] , François Bouchy[14] , Nicolas B. Cowan[15,16] ,
Erica J. Gonzales[17] , David R. Ciardi[18] , Keivan G. Stassun[19,20] , Luc Arnold[21] , Björn Benneke[1] , Isabelle Boisse[22] ,
Xavier Bonfils[23] , Andrés Carmona[23] , Pía Cortés-Zuleta[22] , Xavier Delfosse[23] , Thierry Forveille[23] , Pascal Fouqué[8,21] ,
João Gomes da Silva[24] , Jon M. Jenkins[25] , Flavien Kiefer[4] , Ágnes Kóspál[26,27,28] , David Lafrenière[1] ,
Jorge H. C. Martins[24] , Claire Moutou[8] , J.-D. do Nascimento, Jr.[9,29] , Merwan Ould-Elhkim[8] , Stefan Pelletier[1] ,
Joseph D. Twicken[25,30] , Luke G. Bouma[31] , Scott Cartwright[32] , Antoine Darveau-Bernier[1] , Konstantin Grankin[33] ,
Masahiro Ikoma[13] , Taiki Kagetani[34] , Kiyoe Kawauchi[12,35] , Takanori Kodama[10] , Takayuki Kotani[11,13,36] ,
David W. Latham[9] , Kristen Menou[3,5,6] , George Ricker[37,38] , Sara Seager[37,39,40] , Motohide Tamura[11,13,41] ,
Roland Vanderspek[37] , and Noriharu Watanabe[34]

[1] Université de Montréal, Département de Physique, IREX, Montréal, QC H3C 3J7, Canada; charles.cadieux.1@umontreal.ca
[2] Observatoire du Mont-Mégantic, Université de Montréal, Montréal H3C 3J7, Canada
[3] Department of Physics, University of Toronto, Toronto, ON M5S 3H4, Canada
[4] Institut d'astrophysique de Paris, UMR7095 CNRS, Sorbonne Université, 98 bis bd Arago, F-75014 Paris, France
[5] Department of Physical & Environmental Sciences, University of Toronto at Scarborough, Toronto, ON M1C 1A4, Canada
[6] David A. Dunlap Dept. of Astronomy & Astrophysics, University of Toronto, 50 St. George Street, Toronto, Ontario, M5S 3H4, Canada
[7] Laboratório Nacional de Astrofísica, Rua Estados Unidos 154, Itajubá, MG 37504-364, Brazil
[8] Université de Toulouse, CNRS, IRAP, 14 Avenue Belin, F-31400 Toulouse, France
[9] Center for Astrophysics | Harvard & Smithsonian, 60 Garden Street, Cambridge, MA, 02138, USA
[10] Komaba Institute for Science, The University of Tokyo, 3-8-1 Komaba, Meguro, Tokyo 153-8902, Japan
[11] Astrobiology Center, 2-21-1 Osawa, Mitaka, Tokyo 181-8588, Japan
[12] Instituto de Astrofísica de Canarias (IAC), E-8205 La Laguna, Tenerife, Spain
[13] National Astronomical Observatory of Japan, 2-21-1 Osawa, Mitaka, Tokyo 181-8588, Japan
[14] Departement d'astronomie, Université de Genève, Chemin Pegasi, 51, CH-1290 Versoix, Switzerland
[15] Department of Earth & Planetary Sciences, McGill University, 3450 rue University, Montréal, QC H3A 0E8, Canada
[16] Department of Physics, McGill University, 3600 rue University, Montréal, QC H3A 2T8, Canada
[17] University of California Santa Cruz, Santa Cruz CA 95065, USA
[18] NASA Exoplanet Science Institute-Caltech/IPAC, Pasadena, CA 91125 USA
[19] Department of Physics and Astronomy, Vanderbilt University, 6301 Stevenson Center Lane, Nashville, TN 37235, USA
[20] Department of Physics, Fisk University, 1000 17th Avenue North, Nashville, TN 37208, USA
[21] Canada-France-Hawaii Telescope, CNRS, Kamuela, HI 96743, USA
[22] Aix Marseille Univ, CNRS, CNES, LAM, Marseille, France
[23] Univ. Grenoble Alpes, CNRS, IPAG, F-38000 Grenoble, France
[24] Instituto de Astrofísica e Ciências do Espaço, Universidade do Porto, CAUP, Rua das Estrelas, 4150-762, Porto, Portugal
[25] NASA Ames Research Center, Moffett Field, CA 94035, USA
[26] Konkoly Observatory, Research Centre for Astronomy and Earth Sciences, Eötvös Loránd Research Network (ELKH), Konkoly-Thege Miklós út 15-17, 1121 Budapest, Hungary
[27] Max Planck Institute for Astronomy, Königstuhl 17, D-69117 Heidelberg, Germany
[28] ELTE Eötvös Loránd University, Institute of Physics, Pázmány Péter sétány 1/A, 1117 Budapest, Hungary
[29] Universidade Federal do Rio Grande do Norte (UFRN), Departamento de Física, 59078-970, Natal, RN, Brazil
[30] SETI Institute, Mountain View, CA 94043, USA
[31] Department of Astrophysical Sciences, Princeton University, 4 Ivy Lane, Princeton, NJ 08544, USA
[32] Proto-Logic Consulting LLC, Washington, DC 20009 USA
[33] Crimean Astrophysical Observatory, Department of Stellar Physics, Nauchny, 298409, Crimea
[34] Department of Multi-Disciplinary Sciences, Graduate School of Arts and Sciences, The University of Tokyo, 3-8-1 Komaba, Meguro, Tokyo 153-8902, Japan
[35] Departamento de Astrofísica, Universidad de La Laguna (ULL), E-38206 La Laguna, Tenerife, Spain
[36] Department of Astronomy, School of Science, The Graduate University for Advanced Studies (SOKENDAI), 2-21-1Osawa, Mitaka, Tokyo, Japan
[37] MIT Kavli Institute for Astrophysics and Space Research, Massachusetts Institute of Technology, Cambridge, MA 02139, USA
[38] MIT Department of Physics, Massachusetts Institute of Technology, Cambridge, MA 02139, USA
[39] Earth and Planetary Sciences, Massachusetts Institute of Technology, 77 Massachusetts Avenue, Cambridge, MA 02139, USA
[40] Department of Aeronautics and Astronautics, MIT, 77 Massachusetts Avenue, Cambridge, MA 02139, USA
[41] Department of Astronomy, Graduate School of Science, The University of Tokyo, 7-3-1 Hongo, Bunkyo, Tokyo 113-0033, Japan

[42] Banting Fellow.

Abstract

Exploring the properties of exoplanets near or inside the radius valley provides insight on the transition from the rocky super-Earths to the larger, hydrogen-rich atmosphere mini-Neptunes. Here, we report the discovery of TOI-1452b, a transiting super-Earth ($R_p = 1.67 \pm 0.07\ R_\oplus$) in an 11.1 day temperate orbit ($T_{eq} = 326 \pm 7$ K) around the primary member ($H = 10.0$, $T_{eff} = 3185 \pm 50$ K) of a nearby visual-binary M dwarf. The transits were first detected by the Transiting Exoplanet Survey Satellite, then successfully isolated between the two $3{.}''2$ companions with ground-based photometry from the Observatoire du Mont-Mégantic and MuSCAT3. The planetary nature of TOI-1452b was established through high-precision velocimetry with the near-infrared SPIRou spectropolarimeter as part of the ongoing SPIRou Legacy Survey. The measured planetary mass ($4.8 \pm 1.3\ M_\oplus$) and inferred bulk density ($5.6^{+1.8}_{-1.6}$ g cm^{-3}) is suggestive of a rocky core surrounded by a volatile-rich envelope. More quantitatively, the mass and radius of TOI-1452b, combined with the stellar abundance of refractory elements (Fe, Mg, and Si) measured by SPIRou, is consistent with a core-mass fraction of $18\% \pm 6\%$ and a water-mass fraction of $22^{+21}_{-13}\%$. The water world candidate TOI-1452b is a prime target for future atmospheric characterization with JWST, featuring a transmission spectroscopy metric similar to other well-known temperate small planets such as LHS 1140b and K2-18 b. The system is located near Webb's northern continuous viewing zone, implying that is can be followed at almost any moment of the year.

Unified Astronomy Thesaurus concepts: Exoplanets (498); Super Earths (1655); M dwarf stars (982)

Supporting material: machine-readable table

1. Introduction

Over the past decade, it has become increasingly clear that the typical extrasolar planetary system is quite different from our solar system. Exoplanets are usually found in a much more compact orbital configuration (Howard et al. 2010), and the majority of systems have at least one planet with a size intermediate between the Earth and Neptune (Howard et al. 2012; Fressin et al. 2013). Population studies based on the Kepler sample have shown that the occurrence rate distribution of close-in ($P < 100$ days) exoplanets displays a valley/gap near 1.5–2.0 $R_\oplus$ (Fulton et al. 2017; Fulton & Petigura 2018; Mayo et al. 2018; Hardegree-Ullman et al. 2020). This radius valley most likely separates scaled-up, rocky versions of the Earth (super-Earths) and hydrogen-rich planets reminiscent of Neptune, but smaller (mini-Neptunes). This transition is known to be period-dependent (Van Eylen et al. 2018; Martinez et al. 2019) and to vary with host star properties such as metallicity (Owen and Murray-Clay 2018; Petigura et al. 2018), mass (McDonald et al. 2019; Cloutier & Menou 2020), and age (Berger et al. 2020; David et al. 2021). The existence of a radius valley was rapidly attributed to total or partial photoevaporation of the atmosphere by highly energetic photons during the first 100 Myr, when the host star is more active (Owen & Wu 2013; Lopez & Fortney 2014; Owen & Wu 2017; Lopez & Rice 2018; Wu 2019). However, another atmospheric erosion mechanism is plausible, involving mass loss caused by the release of energy from the planet core, accumulated during formation and slowly cooling down over Gyr timescales (Ginzburg et al. 2018; Gupta & Schlichting 2019, 2020). More recently, Lee & Connors (2021) have shown that the radius valley can be sculpted as a feature of formation, involving gas-poor accretion and supporting the hypothesis of a primordial bimodal distribution, rather than the result of subsequent atmospheric erosion. In order to identify which mechanism dominates, Rogers et al. (2021) predict that the number of well-characterized small exoplanets must reach $\gtrsim$5000. Such characterization requires the precise knowledge of the planetary radii ($\lesssim$5% uncertainty) and, if possible, the planet mass. The combination of the two measurements leads to the mean density of the objects, a way to determine whether their internal structure is compatible with a rocky, gaseous, or intermediate bulk composition.

Identifying new small planets transiting nearby bright stars is the primary objective of the ongoing NASA Transiting Exoplanet Survey Satellite (TESS) mission (Ricker et al. 2015). In operation since 2018, TESS has observed 85% of the celestial sphere, staring for at least ∼27 days at over 50 sectors covered so far ($24° \times 96°$ per sector). The TESS survey has already unveiled more than 5000 candidate exoplanets of which more than 200 have been confirmed as new transiting planetary systems, including small planets around M-dwarf hosts (e.g., TOI-270, Günther et al. 2019; LP 791-18, Crossfield et al. 2019; L 98-59, Cloutier et al. 2019; LTT 1445 A, Winters et al. 2019; LTT 3780, Cloutier et al. 2020a; TOI-1235, Cloutier et al. 2020b; TOI-700, Gilbert et al. 2020; TOI-1266, Demory et al. 2020; LP 714-47, Dreizler et al. 2020; TOI-776, Luque et al. 2021).

M dwarfs represent prime targets not only for TESS, but in exoplanetary science in general. They are the most abundant stars in the solar neighborhood (Reylé et al. 2021) and host on average 2.5 ± 0.2 planets per M dwarf with radii 1–4 $R_\oplus$ (Dressing & Charbonneau 2015). Their smaller size compared to Sun-like stars facilitate the detection and characterization of new exoplanets by producing deeper transits for planets of a given size. The larger planet-to-star mass ratio amplifies the planetary radial velocity (RV) signal, allowing easier mass determination. Lastly, their lower luminosity results in a closer-in habitable zone (HZ), with orbital periods typically of one or two weeks adequately sampled by TESS.

The James Webb Space Telescope (JWST) is poised to revolutionize the field of exoplanet atmospheres (Bean et al. 2018) by offering a collecting area more than 6 times larger than the Hubble Space Telescope (HST) and spectral coverage from the visible to the mid-infrared (0.6–28 μm). JWST will allow simultaneous identification of many chemical species with large absorption cross section in the infrared (e.g., H_2O, CH_4, CO, CO_2, NH_3), as well as probe the atmosphere of terrestrial planets with unprecedented sensitivity. One key objective of TESS is to discover the best transiting exoplanets amenable for atmospheric characterization with JWST (Kempton et al. 2018).

Table 1
TESS Observations of TOI-1452

Sector	Camera	CCD	UT Start Date	UT End Date
14	3	2	2019-07-18	2019-08-14
15	3	2	2019-08-15	2019-09-10
16	2	1	2019-09-12	2019-10-06
17	4	2	2019-10-08	2019-11-02
19	4	1	2019-11-28	2019-12-23
20	4	1	2019-12-24	2019-01-20
21	4	1	2020-01-21	2020-02-18
22	4	4	2020-02-19	2020-03-17
23	4	4	2020-03-19	2020-04-15
24	3	4	2020-04-16	2020-05-12
25	3	3	2020-05-14	2020-06-08
26	3	3	2020-06-09	2020-07-04
40	3	2	2021-06-25	2021-07-23
41	3	2	2021-07-24	2021-08-20
47	4	1	2021-12-31	2022-01-27

Here, we report the discovery of a new small exoplanet around the nearby M dwarf TOI-1452. The planet was first detected by TESS, then characterized via follow-up efforts including RV monitoring with the SPIRou spectropolarimeter. The complete set of observations is described in Section 2. The host star properties and physical parameters are derived in Section 3. Our data analysis and results are presented in Section 4. The implications of this discovery and prospects for follow-up characterization are discussed in Section 5, followed by concluding remarks in Section 6.

2. Observations

2.1. TESS Photometry

TOI-1452 (TIC 420112589) was observed by TESS in sectors 14 through 26 (except 18), thus almost continuously from 2019 July 18 to 2020 July 4, in sectors 40–41 in 2021 from June 25 to August 20, and finally in sector 47 from 2021 December 31 to 2022 January 27 (details in Table 1). TOI-1452 was sampled at the TESS 2 minutes "short" cadence, as the star is part of the cool dwarf list (Muirhead et al. 2018), a specially curated list of high-priority late-K and M dwarfs added to the TESS Input Catalog (TIC; Stassun et al. 2018b, 2019). We used the publicly available[43] per sector light curves produced by the TESS Science Processing Operations Center (SPOC; Jenkins et al. 2016) at NASA Ames, more specifically their Presearch Data Conditioning Simple Aperture Photometry (PDCSAP; Smith et al. 2012; Stumpe et al. 2012, 2014). The PDCSAP light curves are corrected for both instrumental systematic trends seen across stars in the same sector/camera/CCD and for flux contamination from nearby stars located within a few TESS pixels (21″). Flux dilution reduces the observable transit depth, resulting in an underestimation of the planetary radius if not accounted for. This was particularly important for TOI-1452 because a companion star (TIC 420112587; see Section 3.2) is separated by only 3″.2 and has a similar magnitude in the TESS band ($\Delta T = 0.204$). A new background correction was implemented for the TESS extended mission (starting with sector 27). We followed the procedure outlined in the TESS Data Release 38 notes[44] to correct our PDCSAP fluxes from the primary mission (sectors 14–26),
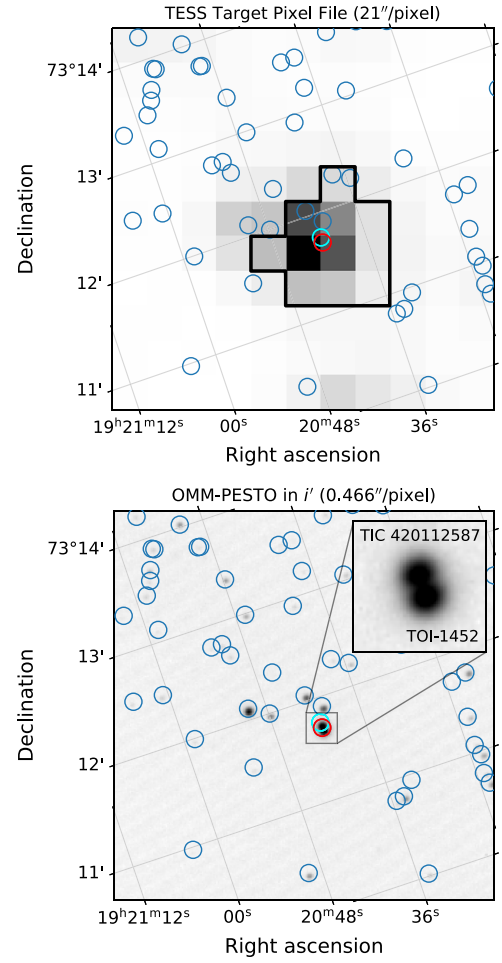

Figure 1. Upper panel: TESS target pixel file of TOI-1452 from sector 14 (11 × 11 pixels subregion). The optimal aperture to extract the PDCSAP photometry is delimited by a black line. Nearby Gaia EDR3 sources are represented with blue circles. TOI-1452 and its 3″.2 companion (TIC 420112587) are shown with a red and a cyan circle, respectively. Lower panel: Same region of the sky observed with OMM-PESTO 1.6 m on 2020 February 22 (see Section 2.2). The visual binary was partially resolved.

adjusting the baseline level and reducing the inferred transit depth by ~1.7%. This ensures that the primary and extended mission data produce the same estimate of the planetary radius. Figure 1 shows an 11 × 11 pixel subregion around TOI-1452 from TESS sector 14 and the same region of the sky observed from the ground. This illustrates how TESS alone cannot resolve the source of a transit between TOI-1452 and the nearby companion TIC 420112587. The normalized PDCSAP light curve of TOI-1452 from sectors 14 and 21 is presented in Figure 2, while the remaining sectors are shown in Figure A1.

A search of the sectors 14–16 with an adaptive, wavelet-based matched filter (Jenkins 2002; Jenkins et al. 2010, 2020) first identified transit signatures for TOI-1452. The data validation reports (DVR; Twicken et al. 2018; Li et al. 2019) fitted a limb-darkened transit model with a signal-to-noise ratio (SNR) of 8.0, a period of 11.06409 days, and an average uncontaminated transit depth of 3.778 parts per thousand (ppt), corresponding to a preliminary planetary radius of $1.83 \pm 0.30 \, R_\oplus$. This led to the announcement of the planet candidate TOI-1452.01 (Guerrero et al. 2021) by the TESS Science Office on 2019 October 26. Simultaneously, the TESS mission announced the candidate TOI-1760.01 around the
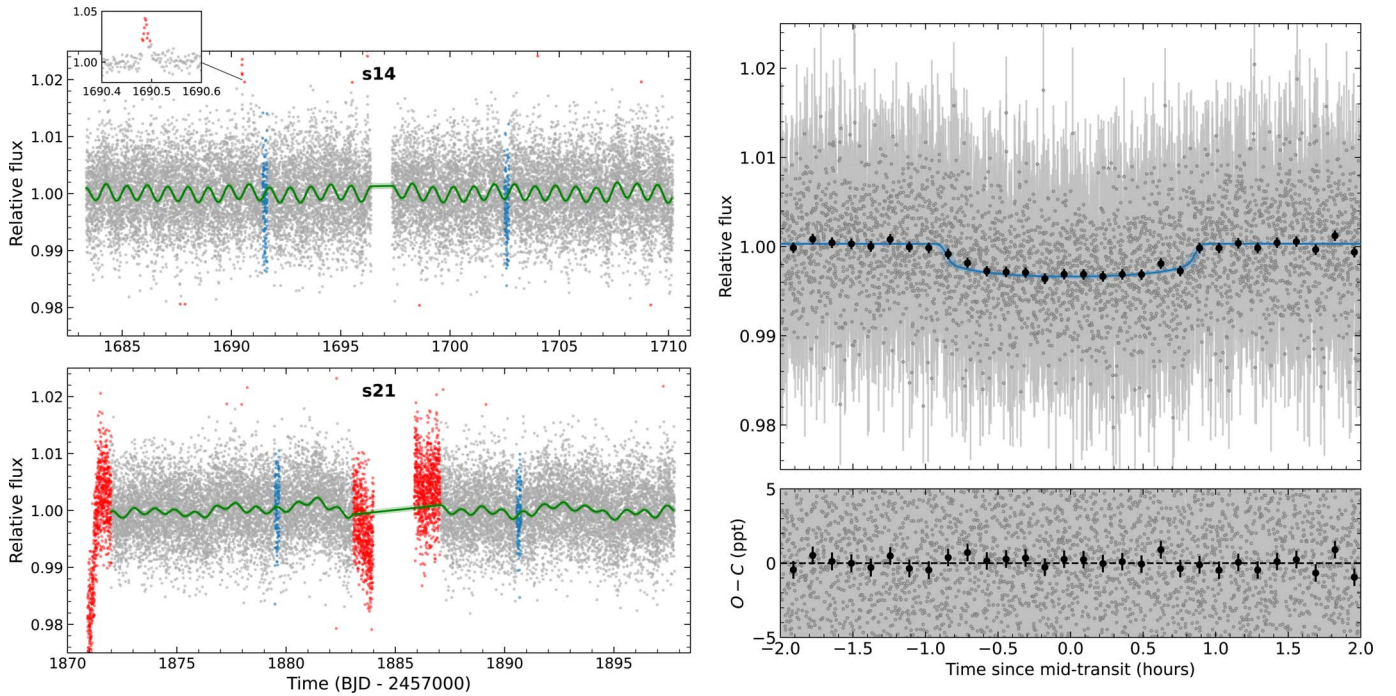

Figure 2. Left panels: Normalized `PDCSAP` light curve of TOI-1452 from sectors 14 and 21, featuring transits (blue data points), a ∼5% stellar flare event (zoomed in subpanel), and outliers (red data points) either rejected by sigma clipping (3.5σ clip) or manually (sector 21). A quasiperiodic Gaussian process model is depicted with the green curve (details in Section 4.2). The remaining sectors are presented in Figure A1. Right panel: TESS phase-folded corrected transits (32) from sectors 14–26, 40–41, and 47. Binned photometry (8 minute phase bin) is represented with black points. The blue curve shows the best-fit transit model (described in Section 4.3), with the 68% confidence interval envelope in light blue. The residuals of this fit are shown below.

companion star TIC 420112587 sharing the same ephemeris as TOI-1452.01. Ground-based photometry was able to isolate the transit signal, originating from TOI-1452 (see Section 4.1). The latest available DVR from sectors 14–41 includes 30 transits and reports a period of 11.06196 days along with a radius $R_p = 1.60 \pm 0.42$ $R_\oplus$. Our complete reanalysis of the TESS light curve presented in Section 4 has resulted in a more precise planetary radius, in agreement with previous estimates. Figure 2 shows the phase-folded 32 transits from currently available sectors. We note that TESS is expected to continue monitoring TOI-1452 during 2022.

2.2. OMM-PESTO Transit Monitoring

Due to the coarse image sampling of TESS (21″ per pixel), the origin of a transit signal may be ambiguous when several stars are located inside the aperture (e.g., Figure 1). For this reason, TESS planet candidates are prone to false positives, occasionally attributed to a nearby eclipsing binary (NEB) contaminating the light curve (Sullivan et al. 2015). Ground-based follow-up with arc-second angular resolution is therefore necessary to validate on-target transit and reject the NEB scenario. For TOI-1452, a particular challenge was to determine the signal's provenance between the target and its 3″2 companion.

Two transit events of TOI-1452.01 were observed using the PESTO camera installed on the 1.6 m telescope of the Observatoire du Mont-Mégantic (OMM), Québec, Canada. PESTO features a 1024 × 1024 pixel EMCCD detector with a pixel scale of 0″466, providing a field of view (FOV) of 7′.95 × 7′.95. We scheduled the two observing sequences with the `TESS Transit Finder` (`TTF`), a customized version of the `Tapir` software package (Jensen 2013), and have used `AstroImageJ` (`AIJ`; Collins et al. 2017) to perform image

calibrations, including bias subtractions and flat field corrections, and differential aperture photometry.

A first full transit was observed on 2020 February 22 in the i' filter with a sequence of 30 s exposure time. As seen in the lower panel of Figure 1, TOI-1452 and TIC 420112587 were partially resolved. Using a circular aperture of 7″9 containing both stars, the transit was detected 53 min earlier than predicted by the `TTF` (2.2σ early), causing us to miss observing a proper pre-ingress baseline (see Figure 3, upper left). Additional TESS data later confirmed that the period was slightly overestimated by SPOC (sectors 14–16 only) at the time of observations, explaining why the transit arrived "early". The transit timing was also later confirmed by TESS sector 22 data, which was contemporaneous to this data set. Even without a proper baseline, this transit was particularly valuable because it allowed us to reject the NEB false-positive scenario and to determine, using point-spread function (PSF) fitting (see Section 4.1), that the signal originated from TOI-1452.

A second full transit of TOI-1452.01 was observed on 2021 March 4 in i', using a 10 s exposure time sequence. With a combined aperture of 8″4, the transit was detected in time according to the `TTF`. In addition to a standard airmass linear detrending (also performed for the first transit), we used the Width (mean of the x- and y-direction FWHM) detrending option in `AIJ`. This was necessary to account for flux loss when the seeing was worse for certain exposures in the sequence, without increasing the aperture radius and dealing with flux contamination from a third star. This made sure that the transit depth was consistent with the one derived from the first PESTO observation, when the overall seeing was better (see Table 2).

The OMM-PESTO observations are summarized in Table 2. The resulting aperture photometry transits are shown in Figure 3 and were included with the 32 TESS transits in our
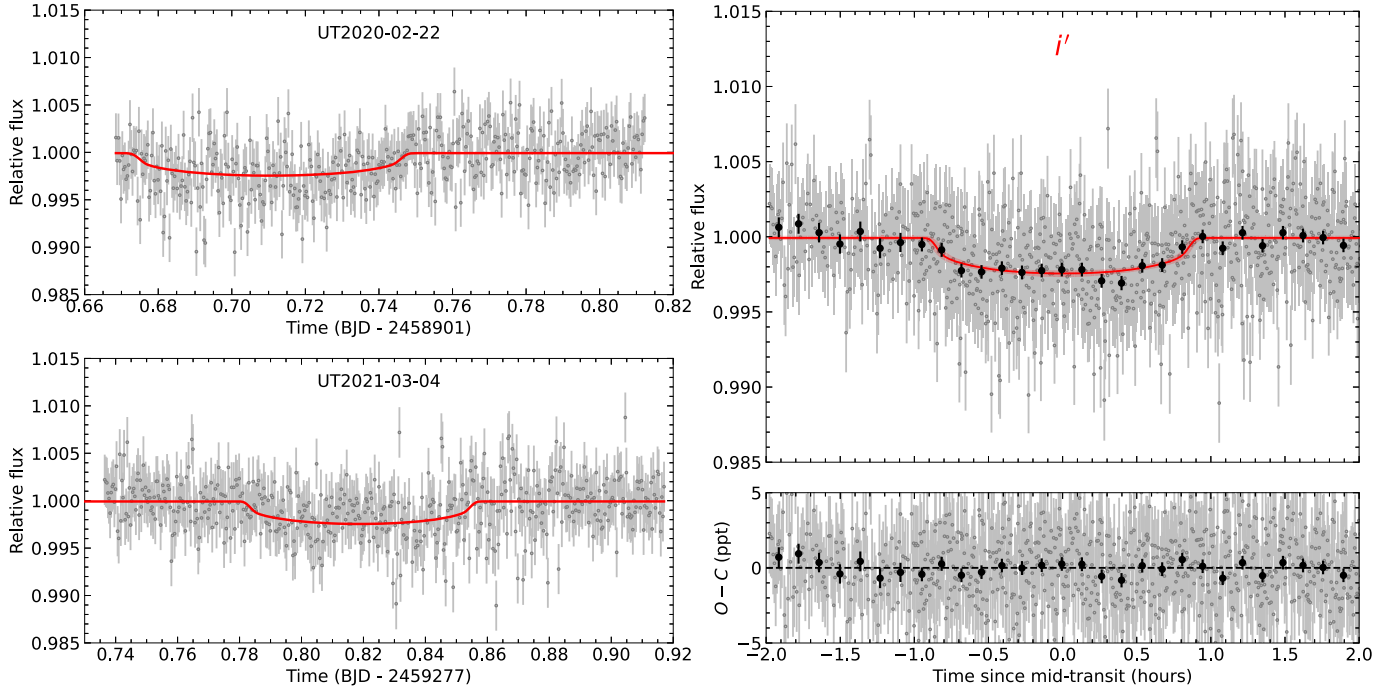
Figure 3. Ground-based transit monitoring of TOI-1452.01 with the PESTO camera installed at OMM. Left panels: Individual transit observations in the i' band on 2020 February 22 UT and 2021 March 4 UT. Right panel: Transits from the left panels folded in phase, with black points representing the binned photometry (8 minute phase bin). The red curve shows the best-fit transit model (described in Section 4.3), with the 68% confidence interval envelope in transparent red. The residuals are shown below the phase-folded transit.

joint analysis (transit and RV data sets) presented in Section 4.3.

2.3. MuSCAT3 Transit Monitoring

A full transit of TOI-1452.01 was observed on 2021 September 8 with the multiband imager MuSCAT3 (Narita et al. 2020) on the 2 m Faulkes Telescope North (FTN) of Las Cumbres Observatory (LCO) at Haleakala observatory, Hawaii. MuSCAT3 has four optical channels, each of which is equipped with a 2 k×2 k CCD camera with a pixel scale of $0\rlap{.}{''}266$ pixel^{-1}, enabling g'-, r'-, i'-, and z_s-band simultaneous imaging. For transit monitoring, significant chromaticity in the transit depths could indicate a diluted eclipsing binary. The exposure times were set at 35, 12, 6, and 3 s for the g', r', i', and z_s bands, respectively. The observations were performed in focus to spatially resolve the host star from the nearby companion star at $3\rlap{.}{''}2$, resulting in the FWHM of stellar point-spread function of 3–8 pixels ($0\rlap{.}{''}8$–$2\rlap{.}{''}0$) depending on the airmass and band (see Table 2).

The obtained images were calibrated by the BANZAI pipeline (McCully et al. 2018). We performed aperture photometry on the calibrated images using a custom pipeline (Fukui et al. 2011) with aperture radii of 5 pixels, or $1\rlap{.}{''}3$, for all bands, which is almost free from flux contamination from the nearby companion star. For each band, we extracted the light curve using different sets of comparison stars but have found that using only the companion (TIC 420112587) as a reference produced the minimum point-to-point dispersion. As both the companion and the target stars have a similar color and are close to each other, the attenuation by the atmosphere is almost identical, so that we can safely assume that any second-order extinction effect (airmass dependent) is almost negligible. We clearly detected the transit on the target star in all bands, as shown in Figure 4, providing further unambiguous evidence

Table 2
Summary of the Ground-based Transit Monitoring of TOI-1452

UT Date	Camera	Filter	PSF FWHM ($''$)	Aperture Size ($''$)
		OMM 1.6 m		
2020-02-22	PESTO	i'	2.9	7.9[a]
2021-03-04	PESTO	i'	3.9	8.4[a]
		LCO-FTN 2 m		
2021-09-08	MuSCAT3	g'	1.8	1.3
2021-09-08	MuSCAT3	r'	1.3	1.3
2021-09-08	MuSCAT3	i'	1.3	1.3
2021-09-08	MuSCAT3	z_s	1.0	1.3

Note.
[a] Using an aperture containing TOI-1452 and TIC 420112587.

that TOI-1452 hosts a transiting object. A summary of this data set is provided in Table 2.

2.4. Keck II/NIRC2 High-resolution Imaging

One or more unresolved sources not in Gaia EDR3 could still be located close to TOI-1452, whether gravitationally bound or not. A blended eclipsing binary (BEB) could indicate a false-positive detection, and any other flux source would lead to underestimate the size of the transiting object in the TESS, PESTO, and MuSCAT3 light curves. For these reasons, we searched for subarcsecond sources around TOI-1452 with the NIRC2 adaptive optics imaging camera installed on the 10 m Keck II telescope. The images were acquired on 2020 May 28 in the K band with a spatial resolution of $0\rlap{.}{''}01$ per pixel, integration time per coadd of 1.6 s, mean PSF FWHM of $0\rlap{.}{''}061$, and airmass of 1.69. Figure 5 shows the 5σ contrast curve of TOI-1452, revealing that no additional companion is
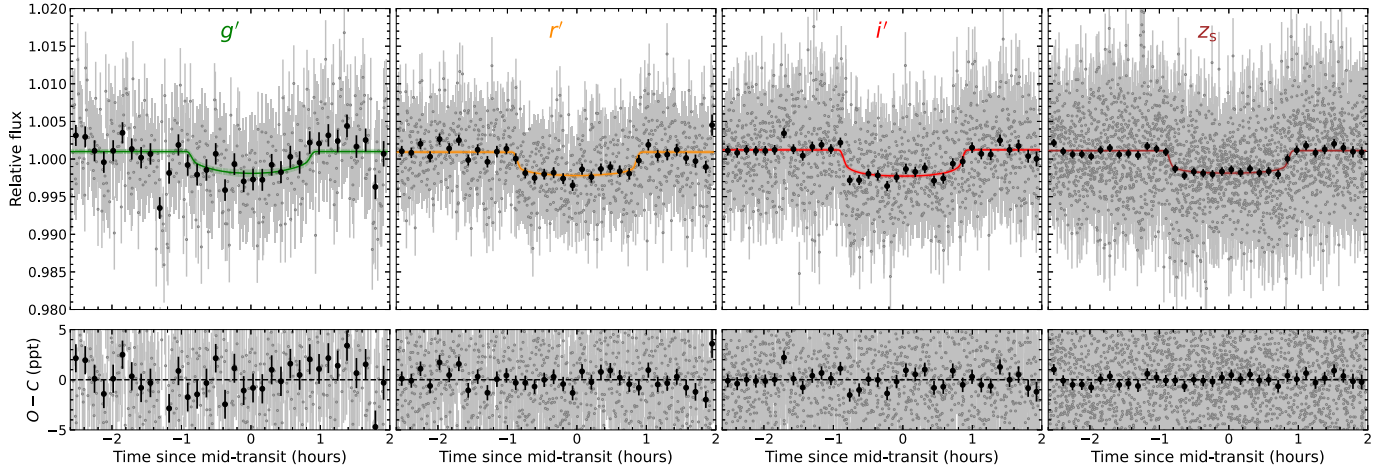
Figure 4. Ground-based transit follow-up of TOI-1452.01 on 2021 September 8 UT with the multifilter (g', r', i', z_s) MuSCAT3 instrument installed on LCO-FTN at Haleakala Observatory. For each corresponding filter, the black points depict the binned photometry (8 minute temporal bin). The color coded curves correspond to each filter's best-fit transit model (described in Section 4.3), with their respective 68% confidence interval envelope in lighter shade. The residuals are shown below each phase-folded transit.

detected with a contrast ratio $\Delta K \leqslant 5.429$ for separation greater than $0\rlap{.}''5$. Although in the K band, this contrast limit is similar to the difference in magnitude required ($\Delta T = 5.55$) for a 50% depth BEB to mimic a 3 ppt transit in the TESS light curve. Following the procedure of Lillo-Box et al. (2014), we calculated the probability of contamination from a blended source due to a random alignment inside $0\rlap{.}''5$. For this, we simulated the galactic stellar population in a region near the target with TRILEGAL (Girardi et al. 2012), using their default bulge, halo, disk (thin and thick) parameters and the log-normal initial mass function of Chabrier (2001). The probability of an undetected source with $\Delta K \leqslant 5.55$ inside $0\rlap{.}''5$ is less than 0.04%, so we can safely assume that the transit signal is not produced by a BEB or significantly diluted by a background star.

2.5. SPIRou Velocimetry

TOI-1452 was observed at 53 epochs from 2020 June 4 to 2020 October 8 with the near-infrared (0.98–2.5 μm) SPIRou spectropolarimeter (Donati et al. 2018, 2020) mounted on the 3.6 m Canada–France–Hawaii telescope (CFHT). The observations were conducted as part of the ongoing SPIRou Legacy Survey (SLS; Donati et al. 2020), more precisely its Transit Follow-up program (SLS-WP2), which aims to characterize exoplanets orbiting low-mass stars revealed by photometric surveys such as TESS. SLS-WP2 has thus far allowed the characterization of the brown dwarf TOI-1278 B (Artigau et al. 2021), the sub-Neptune TOI-1759b (Martioli et al. 2022) transiting M dwarfs, and the studies of the transiting planets HD 189733b (Moutou et al. 2020; Boucher et al. 2021) and AU Mic b (Martioli et al. 2020).

SPIRou offers simultaneous high-resolution spectroscopy and polarimetry, with a spectral resolving power $R \sim 70{,}000$. Each epoch measurement consisted of four consecutive 15 minutes exposures, i.e., a polarimetric sequence, with two rotating Fresnel rhombs varying positions between the exposures. During such a sequence, the two science fibers, A and B, each receive orthogonal polarization states, giving access to the circular polarization and total intensity of the light beam (Stokes V and I). A total of 212 spectra were collected, with SNR per spectral element (~ 2.2 km s^{-1} pixel^{-1} for
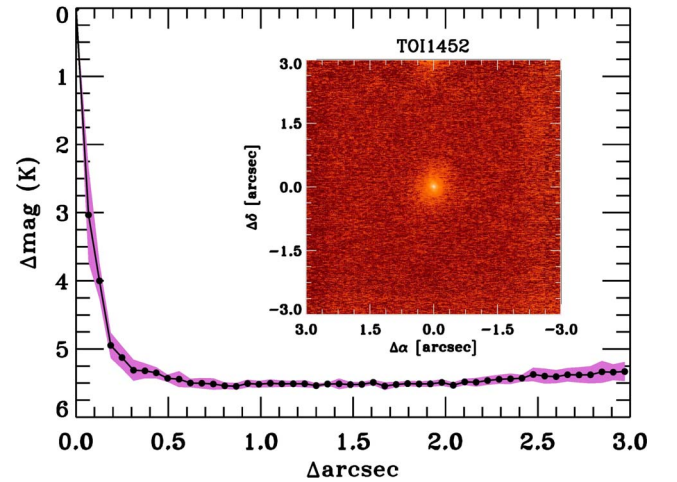

Figure 5. K-band 5σ contrast curve of TOI-1452 from Keck II/NIRC2 adaptive optics imaging. No close companion is detected.

SPIRou) between 20 and 65 (median of 55) near 1.6 μm. Four individual spectra were rejected; one due to loss of guiding, three others because of high extinction (clouds). A single polarimetric sequence of four 15 minute exposures was also acquired on the $3\rlap{.}''2$ companion (TIC 420112587) on 2021 April 22, principally to check its rotation profile and magnetic activity level (see Section 3.5). The diameter of the SPIRou fiber is $1\rlap{.}''33$ and the typical seeing during the observations of TOI-1452 was $0\rlap{.}''8$. We measure no correlation between the radial velocity residuals (Keplerian and activity models described in Section 4.3) and the seeing, suggesting that any effect of contamination from the companion was negligible. Per-epoch RV measurements consisted of taking the error weighted mean of the individual observations within a polarimetric sequence. The data analysis presented in Section 4.3 was performed on the unbinned RVs, but we show the per-epoch average to facilitate visualization.

The SPIRou data were reduced with APERO v0.7.194 (N. J. Cook et al. 2022, in preparation). In brief, APERO starts by correcting known H4RG infrared detector defects (Artigau et al. 2018), then proceeds to identify bad pixels, locate each spectral order on the image, calculate the shape of the

instrument pupil slicer (Micheau et al. 2018), and finally determine from nightly calibration sequences the flat and blaze corrections to apply. Once this preprocessing and calibration step is completed, APERO performs an optimal flux extraction (Horne 1986) in both science channels, separately (fibers A and B) and together (AB), as well as in the simultaneous calibration channel (fiber C). The extracted 2D images (49 orders by 4088 pixels) are then spectral flat fielded, as well as corrected for thermal background and for any leakage from the calibration channel to the science ones. A nightly pixel-to-wavelength solution is applied using a combination of a UNe hollow-cathode lamp and a Fabry–Perot (FP), as described in Hobson et al. (2021). APERO uses the simultaneous FP measurements from fiber C to calculate drifts between individual science frames relative to the nightly wavelength solution (typically below $2 \, \mathrm{m \, s^{-1}}$). Finally, a telluric absorption and night-sky emission correction is applied in a two-step process. The science frames are first pre-cleaned with a TAPAS (Bertaux et al. 2014) absorption model that leaves percent-level residuals for deep ($>50\%$) H_2O and dry absorption features (e.g., CH_4, O_2, CO_2, N_2O, and O_3). Then, a telluric residuals model with 3 degrees of freedom per pixel (optical depths for the H_2O and dry components and a constant) is fitted to the pre-cleaned spectra. The grid of telluric models was generated from a set of rapidly rotating hot stars observed with SPIRou at various airmass, water columns, and dry absorptions, producing telluric-corrected spectra with final residuals at the level of the PCA-based method of Artigau et al. (2014).

Radial velocity measurements were obtained from the telluric-corrected spectra using the novel line-by-line (LBL) method (Artigau et al. 2022). The LBL formalism is based on the Bouchy et al. (2001) framework, in which Doppler shifts are inferred for individual spectral lines ($\sim$16,000 for an M dwarf observed with SPIRou) as opposed to a given spectral range. As in Bouchy et al. (2001), such calculations require a noiseless template as velocities are derived from the comparison between the residuals (observed spectrum minus template) and the derivative of the template. For a given observed star, one uses in practice a high SNR combined spectrum as a template, so that any remaining noise is small compared to that of an individual spectrum. For TOI-1452, the combined spectrum produced by APERO did not reach a SNR as high as other bright standard stars observed in the SLS. Moreover, TOI-1452 is located near the North ecliptic pole, meaning its yearly barycentric Earth radial velocity (BERV) variation is small. Our observations with SPIRou covered BERV excursions between 1.7 and 4.8 km s^{-1}, which is not ideal to filter out telluric lines (i.e., stellar lines do not move a lot with respect to the telluric lines), producing a template that still contains some telluric artifacts. For these reasons, we used the template of Gl 699, a standard star monitored with SPIRou for 2.5 yr with a spectral type (M4V) similar to that of TOI-1452 (M4 $\pm$ 0.5, see Section 3.1) and a good BERV coverage ($\pm$26 km s^{-1}).

For each spectrum, the LBL algorithm combines thousands of per-line velocities into a single RV measurement, with per-line uncertainties varying from 50 m s^{-1} for the strongest features to tens of km s^{-1} for the shallow ones. This is achieved using a simple mixture model: per-line velocities either originate from a Gaussian distribution centered on the mean velocity, with a standard deviation derived from Bouchy et al. (2001), or they arise from another distribution, namely, that of high-sigma outliers, whose plausible causes are diverse

(persisting bad pixels, cosmic rays, telluric residuals, etc.). Lastly, the LBL RVs are corrected for the instrumental day-to-day drift measured by the FP and for a long-term zero-point obtained with a Gaussian process regression using the most observed stars in the SLS. This zero-point calibration is similar to Courcol et al. (2015) for the SOPHIE spectrograph but will be described in more details in a forthcoming publication (T. Vandal et al. 2022, in preparation). The comparison between the LBL and other methods such as the cross-correlation function and template matching is discussed in Martioli et al. (2022) and in Artigau et al. (2022). The final SPIRou radial velocities of TOI-1452 are listed in Table D1, with typical precision of 8.0 m s^{-1} per exposure, or 4.0 m s^{-1} per epoch.

2.6. IRD Velocimetry

Seven high-resolution spectra of TOI-1452 were obtained with the InfraRed Doppler (IRD) spectrograph on the Subaru 8.2 m telescope (Tamura et al. 2012; Kotani et al. 2018) between 2020 September 26 and 2021 June 25. IRD covers the near-infrared wavelengths between 970 nm and 1730 nm, with a spectral resolution $R \sim 70,000$. For accurate RV measurements, stellar spectra were obtained simultaneously with the reference spectra of the laser-frequency comb (LFC). The integration times were set to 600–1500 sec, depending on the available observing time slots and sky conditions. The IRD fiber has a 0″.48 diameter, so that flux contamination from the companion star is not an issue.

The raw IRD data were reduced following the standard procedure of Hirano et al. (2020). We extracted wavelength-calibrated one-dimensional spectra for TOI-1452, as well as for the simultaneously injected LFC. The typical SNR of the TOI-1452 extracted spectra was 60–70 per pixel around 1000 nm. To measure precise RVs for TOI-1452, the reduced spectra were put into the RV analysis pipeline for IRD (Hirano et al. 2020). This pipeline fits each small spectral segment of the observed spectra by the forward-modeling technique, taking into account the instantaneous variations of Earth's atmospheric features as well as the instrumental profile of the spectrograph (which is estimated based on each laser-comb spectrum). The seven IRD RV measurements have an overall precision of 4.0 m s^{-1} and are given in Table D1.

3. Stellar Characterization

3.1. TOI-1452 (TIC 420112589)

The star TOI-1452 (TIC 420112589) is a nearby M dwarf at a distance of 30.504 ± 0.013 pc (Gaia Collaboration et al. 2021). This star does not belong to any known young stellar moving groups, with a very high probability ($>$99.9%) of being a field star (Gagné et al. 2018). The presence of flares and short-period sinusoidal signal in the TESS PDCSAP data (see Figures 2 and A1) cannot be attributed with certainty to TOI-1452, due to flux contamination from multiple nearby objects. An analysis of the photometric variations is presented in Section 4.2, but we note that the polarimetric data from SPIRou reveal no important surface magnetic field variations (see Section 3.5), suggesting that TOI-1452 is relatively quiet, with a rotation period probably much longer than the modulation seen in the TESS light curve.

As discussed in Section 3.4, we measure an effective temperature of 3185 ± 50 K for TOI-1452 using the SPIRou combined spectrum, from which a spectral type (SpT) between

M4 and M4.5 is inferred based on Table 5 of Pecaut & Mamajek (2013). We also considered the Gaia DR2 color to SpT relation of Kiman et al. (2019), more specifically the $G - G_{RP}$ relationship, for an independent SpT determination. From this relationship, the Gaia magnitudes and their respective uncertainties, we obtain a SpT of M3.7 ± 0.6. The same M4 spectral type was derived through a visual comparison of the SPIRou combined spectrum, degraded to a lower resolution ($R \sim 5\,000$), with spectral type standards of the IRTF spectra library (Cushing et al. 2005; Rayner et al. 2009). Considering all these estimates, we adopt a SpT of M4 ± 0.5.

The mass of TOI-1452 was inferred from the Mann et al. (2019) absolute K_s magnitude (M_{K_s}) to $M_\star$ relation for M dwarfs. Taking into consideration the dispersion of this relation, the K_s magnitude, the distance, and their corresponding uncertainties, a mass of $0.249 \pm 0.008\ M_\odot$ is obtained. A similar approach was used to measure the stellar radius, this time using the M_{K_s}–$R_\star$ relationship of Mann et al. (2015), from which we derive $R_\star = 0.275 \pm 0.009\ R_\odot$. Other physical parameters such as the surface gravity ($\log g$), the mean density ($\rho_\star$), and the luminosity ($L_\star$) were determined from the $M_\star$, $R_\star$, and T_{eff} estimates. The stellar parameters of TOI-1452 are summarized in Table 3.

3.2. Bound Companion (TIC 420112587)

TOI-1452 has a resolved companion (TIC 420112587) with several comparable photometric and astrometric measurements. The two objects have similar Gaia EDR3 magnitudes of $G = 13.598 \pm 0.003$ and $G = 13.830 \pm 0.003$ for TOI-1452 and TIC 420112587, respectively. Their Gaia EDR3 parallaxes are identical (within the errors), 32.782 ± 0.014 mas for TOI-1452 and 32.791 ± 0.014 mas for TIC 420112587, indicating a very similar distance to these stars. Their projected angular separation is $3''.182$, which corresponds to a projected physical separation of ~ 97 au, using a common approximate distance of 30.5 pc. The proper motion of TIC 420112587 is similar to that of TOI-1452, with $\mu_\alpha \cos \delta$ and μ_δ within 15% for the two stars (see Tables 3 and 4). TOI-1452 and TIC 420112587 most likely form a visual binary, i.e., a resolved gravitationally bound system, which was previously reported in the TOI visual-binary catalog of Mugrauer & Michel (2020), as well as in the binary catalog based on Gaia EDR3 of El-Badry et al. (2021). From our single visit on the companion star with SPIRou, we measure an RV offset between TOI-1452 and TIC 420112587 of -6.9 km s^{-1}. The SPIRou template spectrum of TIC 420112587 combining only four individual spectra at the same epoch and BERV does not allow for a similar spectral analysis as the one presented for TOI-1452 in Section 3.4.

Using the empirical relationships of Mann et al. (2015, 2019), we obtain a mass of $0.226 \pm 0.006\ M_\odot$ and a radius of $0.254 \pm 0.008\ R_\odot$ for TIC 420112587. The mass ratio of the binary system is close to unity ($q = 0.91 \pm 0.04$), with TOI-1452 as the primary member. The projected physical separation and masses of the two stars imply an orbital period of about 1400 yr. The radial velocity variation expected from such an orbital motion and for a circular orbit is under ~ 1.5 m s^{-1} over the span of our SPIRou RV observations. According to Table 5 of Pecaut & Mamajek (2013) and a $T_{eff} = 3060 \pm 50$ K derived from the spectral energy distribution (see analysis below), TIC 420112587 has an M5 spectral type. The Kiman et al. (2019) $G - G_{RP}$ relationship yields an SpT of M4.0 ± 0.6, so we adopt an intermediate spectral type

Table 3
TOI-1452 Stellar Properties

Parameter	Value	Ref.
Designations		
TIC	420112589	1
TOI	1452	1
2MASS	J19204172+7311434	2
UCAC4	816-023943	3
Gaia EDR3	2264839957167921024	4
Astrometry		
RA (J2016.0)	19:20:41.75	4
DEC (J2016.0)	+73:11:42.35	4
$\mu_\alpha \cos \delta$ (mas/yr)	7.800 ± 0.017	4
μ_δ (mas/yr)	-74.076 ± 0.017	4
π (mas)	32.7823 ± 0.0140	4
Distance (pc)	30.5043 ± 0.0130	4
Stellar parameters		
T_{eff} (K)	3185 ± 50	5
SpT	M4 ± 0.5	5
[M/H]	-0.07 ± 0.02	5
$M_\star$ ($M_\odot$)	0.249 ± 0.008	5
$R_\star$ ($R_\odot$)	0.275 ± 0.009	5
$\log g$ (dex)	4.95 ± 0.03	5
$\rho_\star$ (g cm^{-3})	16.8 ± 1.9	5
$L_\star$ ($L_\odot$)	0.0070 ± 0.0006	5
Photometry		
B	15.94 ± 0.03	1
V	14.35 ± 0.12	1
G_{BP}	15.222 ± 0.004	4
G	13.598 ± 0.003	4
G_{RP}	12.362 ± 0.004	4
T	12.295 ± 0.007	1
g	15.580 ± 0.002	6
r	14.383 ± 0.007	6
i	12.873[a]	6
z	12.272[a]	6
y	11.875 ± 0.020	6
J	10.604 ± 0.058	2
H	10.026 ± 0.058	2
K_s	9.740 ± 0.046	2
W1	8.938 ± 0.023[b]	7
W2	8.760 ± 0.019[b]	7
W3	8.686 ± 0.023[b]	7
W4	8.46 ± 0.29[b]	7

Notes.
[a] The uncertainty was not indicated.
[b] WISE magnitudes include the flux from TOI-1452 and TIC 420112587.
References: (1) TIC (Stassun et al. 2019). (2) Two Micron All Sky Survey (2MASS; Skrutskie et al. 2006). (3) UCAC4 (Zacharias et al. 2013). (4) Gaia EDR3 (Gaia Collaboration et al. 2021). (5) This work. (6) Pan-STARRS1 DR2 (Chambers et al. 2016). (7) AllWISE (Wright et al. 2010).

of M4.5 ± 0.5. A summary of the stellar properties of TIC 420112587 is presented in Table 4.

3.3. Spectral Energy Distribution Fit

As an independent determination of the basic stellar parameters, as well as to estimate the contaminating flux from the nearby companion star, we performed an analysis of the broadband spectral energy distribution (SED) of the stars together with the Gaia EDR3 parallax (with no systematic offset applied; e.g., Stassun & Torres 2021), following the

Table 4
TIC 420112587 Stellar Properties

Parameter	Value	Ref.
Designations		
TIC	420112587	1
TOI	1760	1
2MASS	J19204172+7311467	2
Gaia EDR3	2264839952875245696	3
Astrometry		
R.A. (J2016.0)	19:20:41.76	3
Decl. (J2016.0)	+73:11:45.53	3
$\mu_\alpha \cos \delta$ (mas/yr)	6.845 ± 0.017	3
μ_δ (mas/yr)	-82.216 ± 0.017	3
π (mas)	32.7913 ± 0.0141	3
Distance (pc)	30.4959 ± 0.0131	3
Stellar parameters		
$T_{\rm eff}$ (K)	3060 ± 50	4
SpT	$M4.5 \pm 0.5$	4
$M_\star$ ($M_\odot$)	0.226 ± 0.006	4
$R_\star$ ($R_\odot$)	0.254 ± 0.008	4
$\log g$ (dex)	4.98 ± 0.03	4
$\rho_\star$ (g cm^{-3})	19.5 ± 1.8	4
$L_\star$ ($L_\odot$)	0.0051 ± 0.0005	4
Photometry		
B	15.76 ± 0.17	1
V	13.99 ± 0.2	1
$G_{\rm BP}$	15.512 ± 0.005	3
G	13.830 ± 0.003	3
$G_{\rm RP}$	12.576 ± 0.004	3
T	12.499 ± 0.008	1
g	15.890 ± 0.002	5
r	14.659 ± 0.003	5
i	13.153 ± 0.002	5
z	12.456 ± 0.021	5
y	12.111 ± 0.007	5
J	10.795 ± 0.027	2
H	10.257 ± 0.031	2
$K_{\rm s}$	9.944 ± 0.023	2

Note.
References: (1) TIC (Stassun et al. 2019). (2) 2MASS (Skrutskie et al. 2006). (3) Gaia EDR3 (Gaia Collaboration et al. 2021). (4) This work. (5) Pan-STARRS1 DR2 (Chambers et al. 2016).

procedures described in Stassun & Torres (2016) and Stassun et al. (2017, 2018a). For both stars, we pulled the JHK_S magnitudes from 2MASS, the W1–W4 magnitudes from Wide-field Infrared Survey Explorer (WISE), and the grizy magnitudes from the Panoramic Survey Telescope and Rapid Response System (Pan-STARRS). Together, the available photometry spans the full stellar SED over the wavelength range 0.4–10 μm (see Figure 6). We excluded the WISE photometry from the initial fitting because the two stars are blended in WISE, such that the catalog photometry in fact represents the sum of the fluxes of both stars.

For each star, we performed a fit using NextGen stellar atmosphere models (Hauschildt et al. 1999), with the free parameters being the effective temperature ($T_{\rm eff}$) and metallicity ([Fe/H]). The remaining free parameter is the extinction A_V, which we fixed at zero due to the stars' proximity. The resulting fit for TOI-1452 (Figure 6) has a reduced χ^2 of 1.8 with $T_{\rm eff} = 3100 \pm 50$ K and [Fe/H] $= 0.0 \pm 0.5$. Integrating
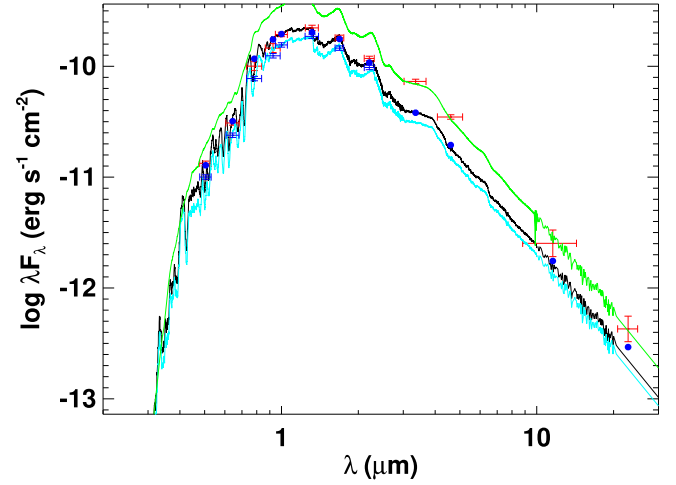

Figure 6. SEDs of TOI-1452 and TIC 420112587 fitted with a NextGen atmospheric model, respectively depicted with a black and a cyan line. Photometric measurements are represented with red (TOI-1452) and blue (TIC 420112587) error bars, where the horizontal bars represent the effective widths of the bandpasses and the small blue dots represent the model fluxes of TOI-1452 for comparison to the red symbols. The WISE measurements (3.4, 4.6, 12, and 22 μm), excluded from this analysis for including both star fluxes, agree with the sum of the two SEDs (green).

the model SED gives the bolometric flux at Earth, $F_{\rm bol} = 2.34 \pm 0.11 \times 10^{-11}$ erg s^{-1} cm^{-2}. Taking the $F_{\rm bol}$ and $T_{\rm eff}$ together with the Gaia parallax, gives the stellar radius, $R_\star = 0.286 \pm 0.011$ $R_\odot$. This independent radius measurement is consistent, although slightly less precise, with the one derived using Mann et al. (2015); $R_\star = 0.275 \pm 0.009$ $R_\odot$.

Similarly, the resulting parameters for the companion star from the SED fit are $T_{\rm eff} = 3060 \pm 50$ K, [Fe/H] $= 0.0 \pm 0.5$, and $R_\star = 0.263 \pm 0.010$ $R_\odot$. This radius estimate is again fully consistent with the value derived from empirical relation ($R_\star = 0.254 \pm 0.008$ $R_\odot$). The sum of the two stellar models is compared to the combined WISE fluxes in Figure 6, showing good agreement. Integrating the companion SED within the TESS bandpass yields a flux ratio (companion relative to TOI-1452) of 0.77 ± 0.03. Note that the flux ratio derived strictly from the T magnitudes from the TIC is 0.829 ± 0.002. In the event that the PDCSAP overestimated the dilution correction for TIC 420112587, this difference in flux ratio would imply a $\sim 1.7\%$ overestimation of the planetary radius.

3.4. Stellar Parameters from SPIRou Spectra

The high-resolution combined spectrum of TOI-1452 from SPIRou lets us determine $T_{\rm eff}$ and the abundance of several elements with relatively good accuracy. This work follows the methodology of F. Jahandar et al. (2022, in preparation), which we briefly summarize here. Because models and observations can often show significant discrepancies (e.g., continuum mismatch in the Y and J bands), we only select for the fitting analysis a subset of relatively strong lines that are matching the models. The selected lines are then divided into several groups of 15 lines, each analyzed independently through a chi-squared fitting routine to infer both $T_{\rm eff}$ and [M/H] for all groups. The spectrum is compared with a grid of ACES models (Allard et al. 2012a; Husser et al. 2013). The advantage of this method is that it yields several (typically 15) independent measurements that can be used to characterize the inherent uncertainties associated with the fitting
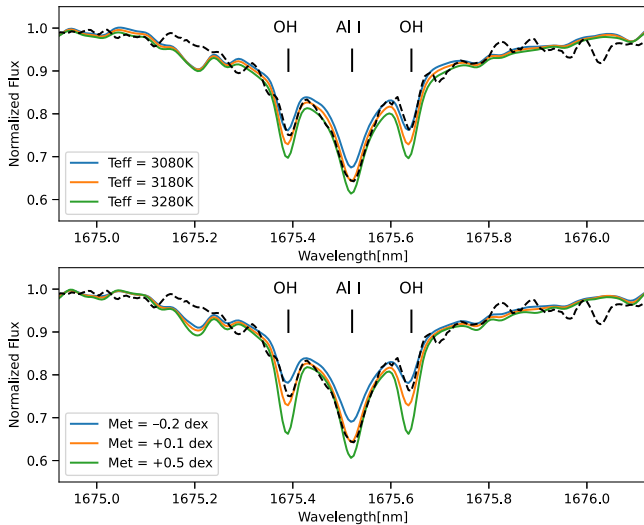
Figure 7. SPIRou observation of the Al I line (1675.514 nm) of TOI-1452 (black dashed line). Top panel: The solid lines represent the ACES models for a fixed metallicity of 0.1 dex and T_{eff} values of 3060 K, 3160 K, and 3260 K. Bottom panel: Same as top panel, but the ACES models have a fixed T_{eff} = 3160 K and metallicity values of -0.2 dex, 0.1 dex and 0.5 dex. These plots illustrate the good sensitivity of near-IR high-resolution spectroscopy for constraining both the metallicity and effective temperature of M dwarfs.

procedure. This analysis applied to the TOI-1452 spectrum yields $T_{eff} = 3185 \pm 50$ K and $[M/H] = -0.07 \pm 0.02$, in good agreement with the parameters derived from the SED fitting analysis. The quoted uncertainty for T_{eff} is internal to our fitting methodology and ignore potential systematic differences with bolometric T_{eff} estimates based on interferometric measurements. While our T_{eff} estimates have yet to be calibrated with bolometric T_{eff}, it is empirically demonstrated that 50–60 K is a typical uncertainty derived from atmosphere models (e.g., Mann et al. 2013, 2015). We thus adopt 50 K for our T_{eff} uncertainty, a conservative value given that the temperature derived from the SPIRou spectrum is inferred from several independent measurements. An illustration of the temperature and abundance sensitivity for an Al I line (at 1675.514 nm) is shown in Figure 7. In practice, several tens of lines are used to derive T_{eff}.

Once T_{eff} is determined, one can then proceed, through a similar procedure, to determine the abundance of all individual lines of a given element. The high-resolution near-infrared spectrum of an M dwarf is characterized by several hundreds of relatively strong OH lines. By selecting only those that are well isolated, i.e., with no known spectral features within a few pixels using the PHOENIX/BT-Settl (Allard et al. 2012b, 2013) and the National Institute of Standards and Technology (Kramida et al. 2021) line lists, we find 72 OH lines, whose individual abundance can be used to quantify the inherent, per-line uncertainty of this method. This uncertainty obviously does not consider any possible systematic errors associated with the ACES atmosphere models. The 72 independent OH abundance measurements are presented in Figure 8, showing a good match with a Gaussian distribution with standard deviation 0.13 dex. For all elements and molecules detected in TOI-1452, we list the average abundance of all lines in Table 5 (see also Figure 9). For chemical species with only one line, we adopt an uncertainty of 0.13 dex from the OH distribution. We report abundances for Fe, Mg, and Si that constitute the bulk material of an exoplanet core and
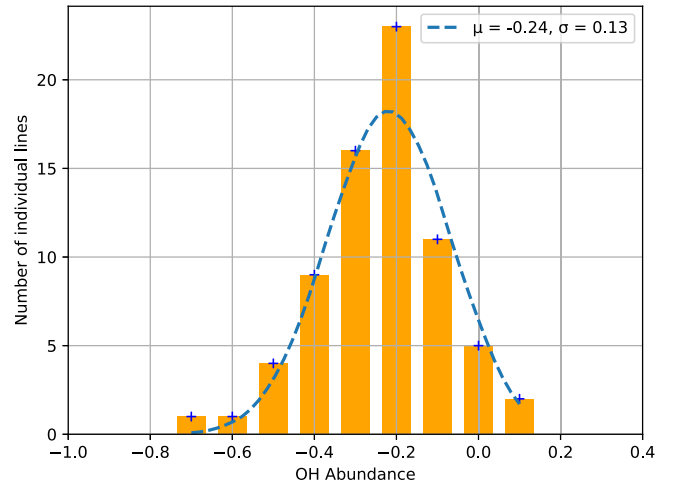

Figure 8. Distribution of OH abundance measurements from 72 isolated OH lines in the SPIRou combined spectrum of TOI-1452. The inherent, per-line uncertainty (0.13 dex) is inferred from a Gaussian fit of this distribution. This uncertainty does not take into account possible systematic errors of the stellar atmosphere models.

Table 5
Stellar Abundance of TOI-1452 for Various Chemical Species Measured by SPIRou

Element	[X/H]	σ	# of Lines
Fe I	-0.07	0.03	38
Al I	0.07	0.11	4
Mg I	0.02	0.07	5
Si I	0.11	0.13	1
Ti I	-0.31	0.06	10
Ca I	0.01	0.12	2
Cr I	0.04	0.06	4
K I	0.03	0.13	1
O I[a]	-0.24	0.02	72
C I	-0.17	0.05	11
N I	-0.12	0.13	1
Na I	-0.22	0.06	2
$<>$[b]	-0.07	0.02	...

Notes.
[a] The oxygen abundance is inferred from OH lines.
[b] Average abundance of all elements.

mantle. The overall metallicity ([M/H]) and its corresponding error are determined by averaging the final abundance of each element in Table 5, assuming a common uncertainty for all elements taken as the median of all individual uncertainties. This approach is chosen to avoid putting too much weight on the oxygen abundance characterized by a small uncertainty.

3.5. Spectropolarimetry with SPIRou

The combination of the four exposures within a polarimetric sequence obtained with SPIRou yields the circular polarization profile at the surface of the star (Donati et al. 2020). The intensity (Stokes I), circular (Stokes V), and null polarization spectra were generated in APERO following the spirou-polarimetry code.[45] We applied the least-square deconvolution (LSD) method of Donati et al. (1997), also outlined in Martioli et al. (2020), to compute the average I and V profiles.

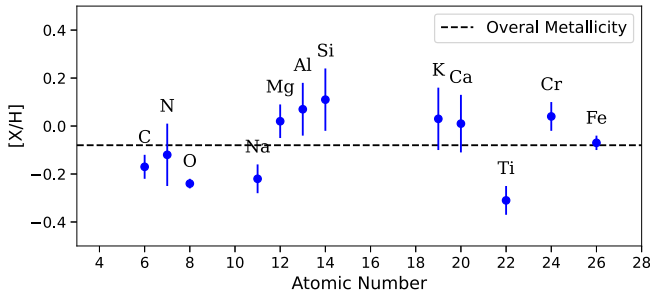---

[45] github.com/edermartioli/spirou-polarimetry

Figure 9. Chemical abundances of 12 different elements via line-by-line spectroscopy of 151 spectral features. The dashed line represents the average metallicity of the star corresponding to the average of all elements.

We used the Vienna Atomic Line Database (Piskunov et al. 1995) and a MARCS atmosphere model (Gustafsson et al. 2008) with $T_{eff} = 3000$ K and $\log g = 5.0$ dex to search for valid atomic features. Lines deeper than 3% and with a known Landé factor were selected to produce a line mask of 955 atomic lines, used in this LSD analysis of TOI-1452. An estimate of the longitudinal magnetic field (B_ℓ) at the stellar surface can then be obtained using Equation (5) of Donati et al. (1997), combining the Stokes I and V LSD profiles, the mean Landé factor of 1.24, and the mean wavelength of 1604.59 nm. By doing this over multiple epochs, one can monitor the large-scale surface magnetic field, expected to vary with the rotation of the star. The polarimetric capabilities of SPIRou can thus serve as a useful activity tracer simultaneous to the RV measurements, as demonstrated in Martioli et al. (2022), where the rotation period of the moderately active M0 star TOI-1759 ($P_{rot} = 35.65^{+0.17}_{-0.15}$ days) was determined from the B_ℓ time series. We obtained independent and consistent values for the B_ℓ of TOI-1452 using the Libre–Esprit pipeline (Donati et al. 1997, 2020) but present below the values from the APERO pipeline.

The B_ℓ time series of TOI-1452 is presented in Figure 10. A simple Lomb–Scargle periodogram analysis shows no obvious periodicity. The B_ℓ data do not favor a sinusoidal model, which could be associated with stellar rotation, over a constant magnetic field (mean $B_\ell = -3.8 \pm 1.8$ G). The small variation of B_ℓ suggests that the field is intrinsically weak (quiet star), or that it is strongly axisymmetric with respect to the rotation axis. Alternatively, the rotation period of TOI-1452 could be longer than the 4 month span of our observations, but this is close to the largest known period for M dwarfs (Newton et al. 2018).

This LSD analysis was also applied on the companion star TIC 420112587 using the single polarimetric sequence acquired with SPIRou. We report a polarimetric signal and a B_ℓ consistent with a null value, indicating that the companion is also probably inactive.

4. Data Analysis & Results

4.1. Determining the Transit Origin with PSF Photometry

The objective of the first OMM-PESTO transit follow-up was to establish the origin of the TESS signal, particularly between the target (TOI-1452) and its companion (TIC 420112587). Standard aperture photometry ruled out any NEB in the FOV but was unable to isolate the transit between the two stars, as they were only partially resolved. We therefore had to rely on a different method using PSF fitting to extract the relative flux of both stars. We used the photutils (Bradley et al. 2020) package to perform the DAOPHOT (Stetson 1987) PSF photometry algorithm. This was achieved by fitting the

PSFs with an effective PSF model (ePSF) generated in photutils using the six stars with the highest SNR in the FOV (excluding our targets), then integrating the best-fit models over pixels containing the stars' signal.

The intent here was not to produce a precise uncontaminated light curve but rather to detect any flux deficit (or excess) that would indicate from which star the transit originates. We thus inspected the TOI-1452 to TIC 420112587 flux ratio as a function of time, normalized to unity outside of transit. The resulting relative light curve is presented in Figure 11 and shows a flux deficit on TOI-1452 during transit. We did not fit a transit model on this light curve, as it is less precise than the one obtained using a combined circular aperture (Figure 3). We nonetheless measure a mean relative flux deficit of 2.33 ± 0.43 ppt, which is an approximation of the uncontaminated transit depth. This flux deficit is comparable in amplitude to the diluted corrected TESS depth (3.31 ± 0.19 ppt) and was detected with a confidence level sufficiently high ($>5\sigma$) to conclude that TOI-1452 was the source of the transit and justify an RV monitoring campaign on this star, starting with SPIRou in June 2020. Later, the MuSCAT3 photometry was able to resolve TOI-1452 and TIC 420112587 and unambiguously identify that the former star hosts a transiting object.

4.2. TESS Light Curve Analysis

The TOI-1452 PDCSAP light curve (Figures 2 and A1) features stellar flares with amplitude of a few percents and ppt-level sinusoidal variations. A strong peak at 0.93 days appears in the Lomb–Scargle periodogram of the multiyear light curve, as well as in all individual sectors. However, computing the autocorrelation function, which is more reliable for accurate photometric rotation period determination (McQuillan et al. 2013), would often find a period of 1.9 days (2×0.93 days) depending on the sector. As the PDCSAP data are corrected for systematic trends, it is unlikely that such corrections significantly perturb those short-term flares and sinusoids. Regardless of the origin of these signals (TOI-1452, TIC 420112587, or any contaminating star), it is crucial to remove the periodic variations to accurately measure the transit parameters. To accomplish this, we adopted a sequential approach where we first correct the PDCSAP data using a Gaussian process (GP), then fit the 32 corrected transits with a model. The details of the GP regression are presented below, while the transit modeling is described in Section 4.3.

We started by masking the epochs of transit and removing outliers from the PDCSAP light curve with sigma clipping. It was determined that a 3.5σ clipping was robust enough to remove both obvious outliers and stellar flares. This sigma clipping removed less than 0.2% of the out-of-transit data. Parts of sectors 21 and 47 coinciding with TESS momentum dump events show large amplitude variations; those were considered to be nonastrophysical and were manually rejected. We also rejected data points in sectors 40 and 41, as they are isolated and have a median considerably different than unity. The data not considered in this analysis are either displayed in blue (transits) or in red (rejected) in Figures 2 and A1. The *cleaned* out-of-transit PDCSAP data set was too large ($N = 237\,634$) to be efficiently modeled with a GP. We therefore binned the data and instead used the corresponding 1 hour effective cadence light curve ($N = 7924$).

The GP regression was done with celerite2 (Foreman-Mackey et al. 2017; Foreman-Mackey 2018). We selected its RotationTerm kernel because it was specifically designed to model a range of quasiperiodic variability, from stellar
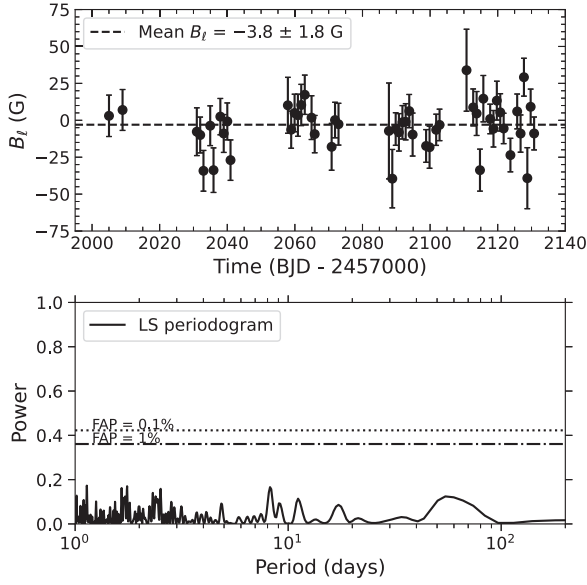
Figure 10. Top panel: Monitoring of the longitudinal magnetic field (B_ℓ) of TOI-1452 with SPIRou. Bottom panel: Lomb–Scargle periodogram of the B_ℓ time series. No clear periodic signal is detected, suggesting a relatively quiet star.
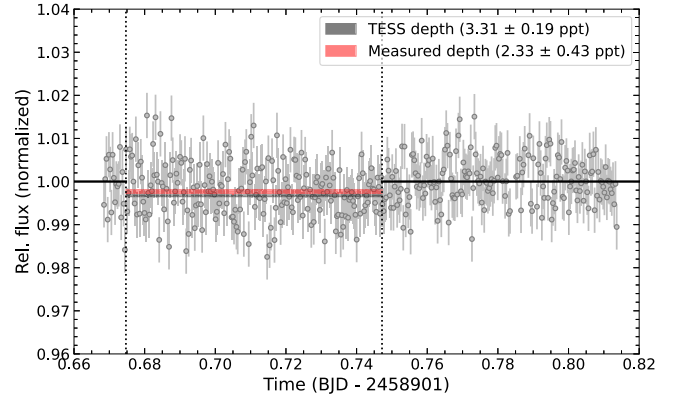

Figure 11. PSF photometry relative light curve (TOI-1452 to TIC 420112587 flux ratio) from OMM-PESTO on 2020 February 22. The dotted black lines represent the ingress and egress of the transit estimated from contemporaneous TESS sector 22 data. The light curve is normalized with the out-of-transit median. A flux deficit comparable to the TESS transit depth is detected on TOI-1452 during transit.

rotation to pulsations. This kernel is the sum of two stochastically driven, damped harmonic oscillator (SHO) terms (`SHOTerm`) capturing both primary (P_{GP}) and secondary ($P_{GP}/2$) modes in Fourier space. The Fourier transform of the covariance function, known as the power spectral density (PSD), takes the following form:

$$S(\omega) = \sqrt{\frac{2}{\pi}} \frac{S_1 \omega_1^4}{(\omega^2 - \omega_1^2)^2 + \omega_1^2 \omega^2/Q_1^2} + \sqrt{\frac{2}{\pi}} \frac{S_2 \omega_2^4}{(\omega^2 - \omega_2^2)^2 + \omega_2^2 \omega^2/Q_2^2}, \quad (1)$$

where each `SHOTerm` PSD is described by their respective power S_1, S_2 at $\omega = 0$, their undamped angular frequency ω_1, ω_2, and their own quality factor Q_1, Q_2.

As the periods of the two oscillators are separated by a factor of 2 ($\omega_2 = 2\omega_1$), the parameterization below reduces by one the number of free parameters:

$$\sigma_1 = \sqrt{S_1 \omega_1 Q_1}, \quad (2)$$

$$\sigma_2 = \sqrt{S_2 \omega_2 Q_2}, \quad (3)$$

$$\tau_1 = \frac{2Q_1}{\omega_1}, \quad (4)$$

$$\tau_2 = \frac{2Q_2}{\omega_2}, \quad (5)$$

$$P_{GP} = \frac{2\pi}{\omega_1} = \frac{4\pi}{\omega_2}, \quad (6)$$

where σ_1, σ_2 are the standard deviations (amplitudes) of the primary and secondary modes, τ_1, τ_2 are the damping timescales of the primary and secondary oscillations, and P_{GP} is the undamped period of the primary mode. Note that these parameters differ slightly from the default `RotationTerm` kernel parameterization by making no assumptions on the relative amplitudes and quality factors between the two modes.

Our `PDCSAP` GP model consisted of the five hyperparameters above, plus an excess white noise term s. We sampled the posterior distributions of the parameters in their logarithmic form $\{\ln \sigma_1, \ln \sigma_2, \ln \tau_1, \ln \tau_2, \ln P_{GP}, \ln s\}$ using the Markov chain Monte Carlo (MCMC) package `emcee` (Foreman-Mackey et al. 2013) and a Bayesian formalism. We employed 100 walkers and performed 100,000 steps with a burn-in of 10,000. The number of steps was greater than 50 times the autocorrelation timescale for each parameter, which usually indicates a sufficient level of convergence (Sokal 1997; Foreman-Mackey et al. 2019). The adopted prior distributions and the posteriors median, 16th and 84th percentiles are reported in Table 6. The resulting mean GP prediction is shown in Figures 2 and A1 superimposed on the original `PDCSAP` cadence. Even though the sinusoidal variations visually appear to repeat every ~0.93 day, our model converged to a very well constrained primary oscillation of 1.8680 ± 0.0004 days, thus indicating significant power at the second harmonic.

It is beyond the scope of this study to assess the exact cause of this strong and persistent signal, but we showed earlier that the SPIRou magnetic field constraints of TOI-1452 are inconsistent with a fast rotator and active object. Moreover, a 1.9 days rotation period for TOI-1452 would correspond to a $v \sin i$ of ~7 km s^{-1}, readily detectable in the SPIRou combined spectrum. Instead, the mean line profile FWHM measured from the cross-correlation function (CCF) calculated in `APERO` suggests a slow rotator (i.e., $v \sin i < 2$ km s^{-1}). We repeated this step for the companion star from the single visit with SPIRou and also measured a FWHM consistent with $v \sin i < 2$ km s^{-1}. Thus, the rotation of the companion star is also most probably not causing this photometric signal.

4.3. Joint Transit RV Fit

In order to constrain the physical and orbital parameters of TOI-1452b, we conducted a joint analysis of the transits (TESS, OMM-PESTO, and MuSCAT3) and the RV data (SPIRou and IRD). The joint fit was performed using the `juliet` (Espinoza et al. 2019) package, which utilizes `batman` (Kreidberg 2015) to generate transit models and `radvel` (Fulton et al. 2018) to compute Keplerian RV models. The `juliet` framework implements nested sampling algorithms to sample posterior distributions, while also enabling

Table 6
Prior and Posterior Distributions of the Quasiperiodic GP Model of the TOI-1452 TESS Light Curve (Details in Section 4.2)

Parameter	Prior	Posterior
$\ln \sigma_1$	$\mathcal{U}(-10, 0)$	$-7.5^{+0.5}_{-0.5}$
$\ln \sigma_2$	$\mathcal{U}(-10, 0)$	$-7.1^{+0.5}_{-0.4}$
$\ln [\tau_1/\mathrm{days}]$	$\mathcal{U}(-10, 10)$	$-1.42^{+0.13}_{-0.14}$
$\ln [\tau_2/\mathrm{days}]$	$\mathcal{U}(-10, 10)$	$7.1^{+1.1}_{-0.8}$
$\ln [P_{\mathrm{GP}}/\mathrm{days}]$	$\mathcal{U}(-2, 5)$	$0.6248^{+0.0002}_{-0.0002}$
$\ln s$	$\mathcal{U}(-15, 0)$	$-12.7^{+1.6}_{-1.5}$

Note. $\mathcal{U}(a, b)$ is the uniform distribution between values a and b.

model comparison via evaluations of the Bayesian log-evidence ($\ln Z$). We chose the dynesty (Speagle 2020) dynamic nested sampling option in juliet. Standard nested sampling (Skilling 2006) was designed to estimate evidences, not posteriors, and thus struggles with parameter estimation for complex distributions. Dynamic nested sampling (Higson et al. 2019), on the other hand, adapts the number of live points based on the structure of the posteriors, providing parameter estimation comparable to MCMC algorithms.

The transit and RV components of the joint fit have four parameters in common: the orbital period P, the time of inferior conjunction t_0, the eccentricity e, and the argument of periastron ω. For the transit modeling, we followed the parameterization from Espinoza (2018) of the impact parameter b and the planet-to-star radius ratio $p = R_{\mathrm{p}}/R_{\star}$ to efficiently sample physically plausible values in the (b, p) space. Instead of fitting the scaled semimajor axis $a/R_{\star}$, we used the stellar density $\rho_{\star}$ parameterization available in juliet. Fitting $\rho_{\star}$ takes into account any prior information on the stellar mass and radius. We adopted a Gaussian prior on $\rho_{\star}$ using the value and uncertainty in Table 3. Stellar limb-darkening effects in TESS, OMM-PESTO, and MuSCAT3 transits were modeled using the quadratic q_1 and q_2 parameters defined in Kipping (2013). For each instrument, we included in juliet a flux dilution factor D, a baseline flux M, and an extra jitter term σ. We set D_{TESS} to 1 (no dilution), as the PDCSAP data are already corrected for crowding effects. The OMM-PESTO light curve combines the flux of TOI-1452 and TIC 420112587, which requires an adequate D_{PESTO} factor to compensate for contamination. We thus constructed a Gaussian prior on D_{PESTO} with a mean value calculated with Equation (6) of Espinoza et al. (2019) and flux ratio derived from TOI-1452 and TIC 420112587 magnitudes in the i band (from Tables 3 and 4). The adopted prior on D_{PESTO} was $\mathcal{N}(0.564, 0.0564^2)$, that is, with a 10% standard deviation to account for errors on the magnitudes and deviations between i and i'. We also explored fixing D_{PESTO} to 0.564, while letting D_{TESS} vary freely between 0 and 2. Both approaches yielded a consistent measurement of the planetary radius (within 1σ), indicating that the PDCSAP fluxes were in all likelihood properly corrected for contamination. The dilution in the MuSCAT3 light curves was a priori unknown. However, it is expected that the g' transit was more affected by dilution, as the seeing was worse for this filter (see Table 2). We adopted a conservative approach where a different D_{MuSCAT3} is applied for each filter, with uniform priors between 0.5 (twice the flux) and 1.

The parameters specific to the RV Keplerian component were the semi-amplitude K, per-instrument offsets γ, and extra white noise terms σ. We explored adding a global GP to model

common stellar activity signal in the SPIRou and IRD data. For this, we used the GP implementation in juliet that runs celerite (Foreman-Mackey et al. 2017). We chose the Matérn-3/2 approximation kernel, which takes the following form:

$$k_{i,j}(\tau) = A_{\mathrm{GP}}^2 [(1 + 1/\epsilon)e^{-(1-\epsilon)w}(1 - 1/\epsilon)e^{-(1+\epsilon)w}], \quad (7)$$

where $\tau = |t_i - t_j|$ is the time interval between data points i and j, A_{GP} is amplitude of the GP, $w = \sqrt{3}\,\tau/\ell_{\mathrm{GP}}$, with ℓ_{GP} the timescale of the GP, and ϵ is set to 0.01 (when $\epsilon \to 0$, $k_{i,j}$ converges to a Matérn-3/2 kernel). We did not fit a per-instrument A_{GP} and ℓ_{GP} due to the limited number of RV measurements from IRD. We also considered choosing a quasiperiodic kernel in celerite instead (Equation (56) of Foreman-Mackey et al. 2017). As no clear periodicity was detected in the B_{ℓ} time series, or other activity indicators from the LBL such as the dLW metric (Zechmeister et al. 2018) or chromatic velocity slope changes, we applied a uniform prior on the stellar rotation period, namely, $\mathcal{U}(0.1, 120)$ days. We found that the Matérn-3/2 kernel gave equivalent results with fewer hyperparameters needed (two instead of four) and that the quasiperiodic GP did not converge to a specific rotation period, showing no preference for a period of 0.93 days (or 2 ×0.93 days) as seen in TESS photometry. This is another indication that the sinusoidal signal in the out-of-transit PDCSAP data is probably not associated with TOI-1452 stellar activity.

We examined the change in Bayesian log-evidence for a suite of joint models ($\mathcal{M}$), all having an identical transit component. The "zero"-planet model ($\mathcal{M}_{\mathrm{0p}}$) has a K fixed to $0\,\mathrm{m\,s}^{-1}$, with only the RV offsets and extra white noise terms allowed to vary. This model tests whether the RV dispersion can be fully explained by white noise only, without questioning the transit detection. Single-planet models can either be with circular ($\mathcal{M}_{\mathrm{1cp}}$; $e = 0$, $\omega = 90°$) or eccentric orbits ($\mathcal{M}_{\mathrm{1ep}}$; free e, ω). Two additional models include a global RV activity GP ($\mathcal{M}_{\mathrm{1cp+GP}}$ and $\mathcal{M}_{\mathrm{1ep+GP}}$). To objectively assess the contribution from the IRD observations, we decided to apply this framework first on the SPIRou data individually and then using the full RV data set (SPIRou + IRD).

For two competing models, the difference in log-evidence ($\Delta \ln Z$) informs on the probability that one model supports the data better than the other. To interpret the significance of the $\Delta \ln Z$ and select the "best" model, we followed the empirical scale introduced in Table 1 of Trotta (2008). A $\Delta \ln Z > 5$ translates into "strong" evidence toward the model with the highest $\ln Z$. A $2.5 < \Delta \ln Z < 5$ corresponds to "moderate" evidence, while $\Delta \ln Z \leqslant 2.5$ shows "weak" evidence at best, i.e., neither model should be favored in that case.

Figure 12 shows the Bayesian log-evidence for different joint models and data sets. Note that the typical errors on the $\ln Z$ computed by dynesty were 0.5, so that the $\Delta \ln Z$ presented in Figure 12 have associated uncertainties of 0.7. We first observe that all planetary models are strongly favored ($\Delta \ln Z > 5$) compared to the "zero"-planet solution ($\mathcal{M}_{\mathrm{0p}}$), providing quantitative evidence that the TOI-1452b Keplerian signal is detected in velocimetry, in phase with transit. There is also compelling evidence for models with an RV activity GP ($\mathcal{M}_{\mathrm{1cp+GP}}$ and $\mathcal{M}_{\mathrm{1ep+GP}}$), increasing $\ln Z$ by approximately 10 relative to $\mathcal{M}_{\mathrm{1cp}}$ and $\mathcal{M}_{\mathrm{1ep}}$. However, considering only the
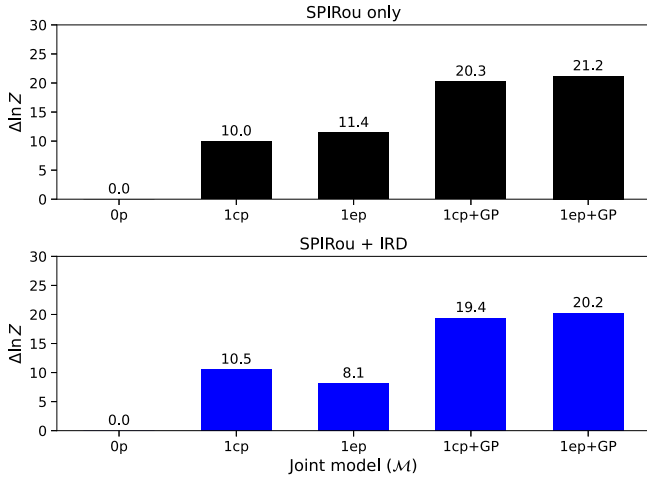
Figure 12. Bayesian log-evidence ($\ln Z$) for different joint transit RV models ($\mathcal{M}$) and RV data sets. The typical uncertainty on the $\Delta \ln Z$ is 0.7. The "zero"-planet model $\mathcal{M}_{0p}$ has a fixed $K = 0$ m s^{-1}. Single-planet models $\mathcal{M}_{1cp}$ and $\mathcal{M}_{1ep}$ correspond to an RV component with a circular ($e = 0$, $\omega = 90°$) or eccentric (free e, ω) orbit, respectively. Models $\mathcal{M}_{1cp+GP}$ and $\mathcal{M}_{1ep+GP}$ add a Gaussian process to remove correlated noise in the RV data.

SPIRou data yields similar or slightly larger $\Delta \ln Z$ for all $\mathcal{M}$ compared to joint fits that include the seven IRD RVs. This suggests that the IRD observations do not significantly contribute to improve the Keplerian solution for TOI-1452b. The median RV uncertainty from IRD (4.03 m s^{-1}) is nearly identical to SPIRou (4.00 m s^{-1}), but the point-to-point scatter (rms) is much larger: 12.71 m s^{-1} for IRD and 5.76 m s^{-1} for SPIRou. The models fail to capture the extra rms in the IRD data and are instead converging to solutions with white noise term comparable to the overall scatter (see Table B1). This is apparent in Figure 13 showing the RV component of the joint fit (model $\mathcal{M}_{1cp+GP}$) using the full data set, with each instrument having their original error bar plotted. The IRD radial velocities were produced using the template spectrum of TOI-1452. As previously mentioned, this star has a small BERV excursion, which is not ideal for filtering out telluric lines. This may explain the increased dispersion in the resulting RVs, in this case, at a level much larger than the Keplerian signal. For this reason, we opted to present below the results using only the SPIRou RVs. We nonetheless provide all the relevant parameters of the RV modeling for the SPIRou only and SPIRou+IRD data sets in Table B1.

The eccentric model $\mathcal{M}_{1ep+GP}$ produced the highest $\ln Z$ (Figure 12) but with a Bayesian evidence indistinguishable from the circular model $\mathcal{M}_{1cp+GP}$ ($\Delta \ln Z = 0.9$). We report an eccentricity of $0.12^{+0.12}_{-0.08}$, with $e < 0.32$ at a 95% confidence, but argue that the simpler, circular model should be preferred at this point. The adopted priors and resulting posteriors of the $\mathcal{M}_{1cp+GP}$ fit are summarized in Table 7. The MuSCAT3 photometric parameters are given in another table (Table 8) to facilitate comparison between filters. We measure dilution factors D for MuSCAT3 consistent with no dilution for the i' transit, with a moderate level of contamination ($\sim$30%) in the g' band. If we assume instead that the flux dilution was exactly zero for all filters, the uncorrected transit depths ($\delta_{\text{uncorr.}}$) presented in Table 8 show no sign of strong chromaticity. The best-fit transit models of the TESS, OMM-PESTO, and MuSCAT3 photometry are shown in Figures 2, 3, and 4, respectively. The best circular ($\mathcal{M}_{1cp+GP}$) and eccentric

($\mathcal{M}_{1ep+GP}$) RV orbital fits of TOI-1452b are shown in Figure 14 in a phase-folded format.

5. Discussion

5.1. Planet Composition

The analysis of the transit and RV data yields a mass of $4.82 \pm 1.30\,M_\oplus$ and a radius of $1.672 \pm 0.071\,R_\oplus$, which together convert into a planetary bulk density of $5.6^{+1.8}_{-1.6}$ g cm^{-3}. A density similar to that of the Earth (5.5 g cm^{-3}) for a planet that has more mass is indicative of an object composed of lighter material. We placed these measurements in a mass–radius diagram (Figure 15), along with various theoretical composition curves obtained by the interior structure model of Valencia et al. 2007, 2013; Plotnykov & Valencia 2020. We populated this diagram, and the figures in the discussion below, with data from the NASA Exoplanet Archive (Akeson et al. 2013) using the `exofile` tool.[46]

By comparing the mass and size of TOI-1452b to theoretical mass–radius curves in Figure 15, we see three possibilities for the nature of this planet: (1) an ocean planet, (2) a bare rock with an iron content less than that of Earth, or (3) a terrestrial planet with a thin, low molecular weight atmosphere (e.g., H–He). The water world hypothesis is supported by a temperate equilibrium temperature for TOI-1452b of 298 ± 6 K assuming an Earth-like Bond albedo ($A_B = 0.3$), and between 226 and 326 K for extreme A_B of 0.77 (Venus-like) and 0 (pure absorber). The insolation level of TOI-1452b is about 80% higher than the Earth ($S = 1.8 \pm 0.2\,S_\oplus$), similar to Venus ($S = 1.91\,S_\oplus$).

Focusing on the first two possibilities, we used an MCMC approach (`emcee`; Foreman-Mackey et al. 2013) coupled to an interior structure model (Valencia et al. 2007) to obtain the distribution of mass fractions of iron and water that are consistent with the data. The details of this modeling can be found in Plotnykov & Valencia (2020). The H_2O layer is described by the equation of state from Hemley et al. (1987) and Stewart & Ahrens (2005). We report below the 16th, 50th, and 84th percentiles of the posterior distributions (available in Appendix C).

From the chemical analysis of the star (Section 3.4), we obtain chemical ratios relevant to the planetary interior. Notably, TOI-1452 might have a slightly lower Fe/Mg weight ratio compared to the Sun (see Table 9), but in fair agreement with that of a sample of $\sim$1000 M dwarfs from the APOGEE (DR16) catalog (Majewski et al. 2016; Ahumada et al. 2020) with known chemical ratios (see Figure 16). The APOGEE abundances are derived from high-resolution near-infrared spectroscopy ($R \sim 22\,000$), with typical uncertainty on [Fe/H] and [Mg/H] of 0.02 dex. Obtaining the Si ratios for TOI-1452 was difficult given the scarcity of spectral lines. In addition, we derive a C/O weight ratio consistent with the solar value. Our chemical abundance ratios for TOI-1452 are summarized in Table 9.

To infer the planet's composition for scenarios 1 and 2, we can either make no assumptions on the refractory ratios, and thus, obtain all possible compositions that fit the mass–radius data; or, assume that the refractory ratios of planet and star are related, and use the star's ratios as priors in the Bayesian analysis. Given that the refractory ratios of super-Earths seem

---

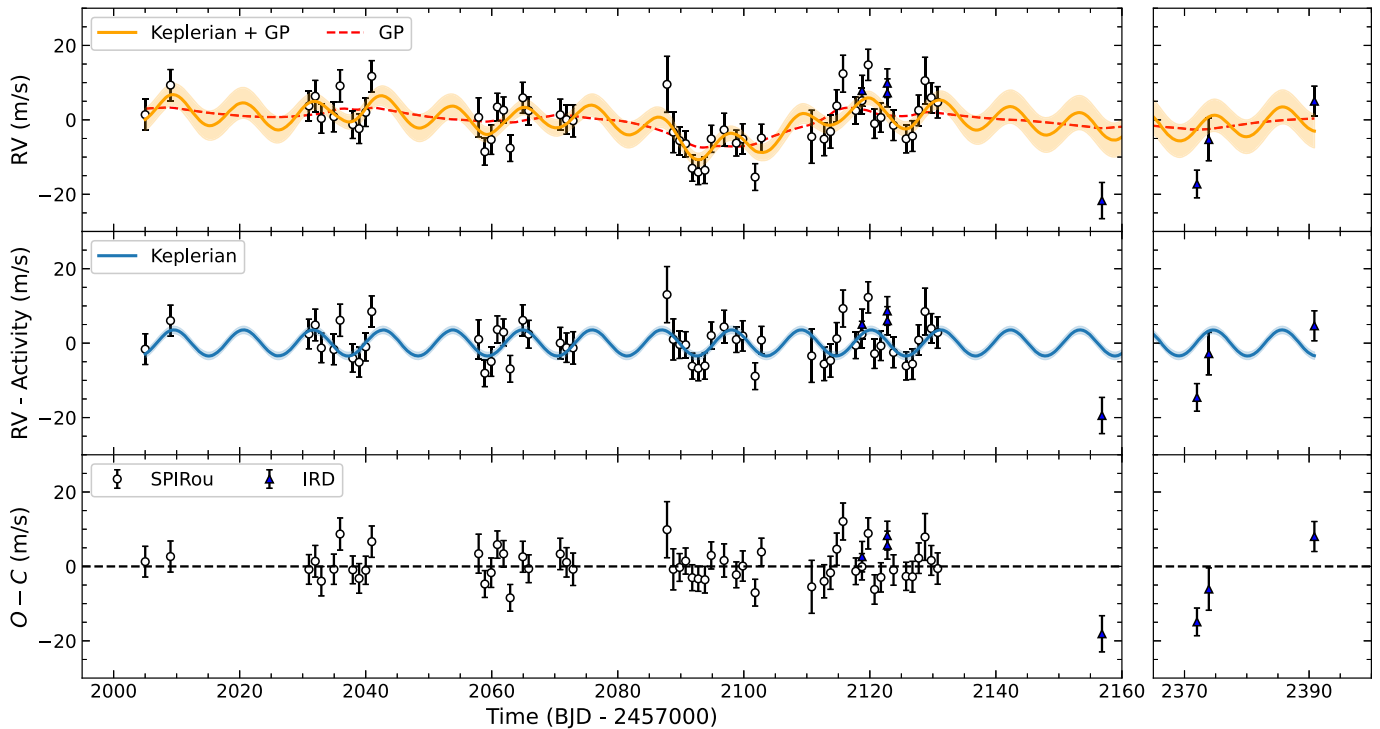[46] github.com/AntoineDarveau/exofile

Figure 13. RV time series from SPIRou and IRD with the best-fit Keplerian + activity GP (orange curve), activity GP-only (red dashed curve), and Keplerian-only (blue curve) models overplotted. The residuals below show an overall agreement between the SPIRou errors and the RV dispersion, which is difficult to assess for IRD given the limited number of measurements.

to span a larger range than that of stars (Plotnykov & Valencia 2020), we applied both methods here. In both cases, we kept the Mg/Si ratio in the planetary mantle the same as the star. This assumption should not affect the results considerably, given that the mantle minerals formed by different Mg/Si ratios have similar equations of state and thus, the relative content of Mg to Si is not constrained by planetary mass and radius data (Plotnykov & Valencia 2020).

In the case where we make no assumptions, we obtain a water-mass fraction (WMF) of $0.27^{+0.20}_{-0.15}$ and core-mass fraction (CMF) of $0.30^{+0.20}_{-0.17}$. These values translate to Fe/Si $= 2.9^{+5.4}_{-1.9}$ and Fe/Mg $= 3.4^{+6.3}_{-2.2}$ by weight. The planetary refractory ratios are particularly large primarily due to large uncertainty in planetary mass but also the degeneracy that ensues when considering water. The tail of the Fe/Mg distribution is long because this case allows for little to no mantle in the planet (see Figure C1). If instead, we assume the refractory ratios of the star as priors, we obtain lower water- and core-mass fractions: WMF $= 0.22^{+0.21}_{-0.13}$, CMF $= 0.18 \pm 0.06$, resulting in Fe/Si $= 1.3 \pm 0.4$ and Fe/Mg $= 1.5 \pm 0.4$. Both abundance scenarios yield a nonzero, yet poorly constrained, WMF. The large uncertainty on both the CMF and WMF is rooted to the modest mass constraint (3.7σ). Better mass measurements are needed to confirm that TOI-1452b has a significant WMF.

A different possibility (scenario 2 discussed above) is that this planet is a bare rock with no significant atmosphere, perhaps because it lost any acquired water through atmospheric evaporation during the high-insolation phase of the M dwarf host star (Barnes & Heller 2013; Bolmont et al. 2017). In this case, we constrain the physical model solutions but make no assumptions on the refractory ratios. The results show a CMF $= 0.19^{+0.18}_{-0.12}$, with Fe/Si $= 1.0^{+1.0}_{-0.5}$ and Fe/Mg $= 1.2^{+1.2}_{-0.6}$ by weight. This CMF

indicates a planet not as dense as the Earth, with refractory ratios still consistent at the 1σ level with those of its host star (see Table 9 and Figure 16). However, the maximum a posteriori estimate of Fe/Mg ($\sim$0.8) for this bare rock scenario is lower than that of its host star. Forming planets that are iron poor with respect to their host star is difficult (Scora et al. 2020). Therefore, based on our current knowledge of planet formation and the chemical characteristics of the star, this scenario is less likely.

A summary of this interior modeling is presented in Table 9 and Figure 16. The posterior distributions for the three models (no assumptions, stellar priors and bare rock) are shown in Appendix C.

Outside of these scenarios, our observations do not rule out other structures with a low molecular weight atmosphere (scenario 3) such as an Earth-like interior surrounded by an H–He envelope at $T = 300$ K containing $\sim$0.1% of the total mass (up to 0.5% H–He at 1σ). One way to firmly break the degeneracy in planetary internal structures would be to characterize the atmosphere of TOI-1452b.

5.2. Atmospheric Characterization Prospect

TOI-1452b is a prime target for follow-up transit spectroscopy with JWST. The system is located near Webb's continuous viewing zone (CVZ), more precisely at a few degrees ($\sim$10°) off the Northern CVZ, which means that it could be observed most of the year. Moreover, TOI-1452b is one of the few identified super-Earths in a temperate regime (T_{eq} between 200 and 400 K) orbiting a relatively bright star amenable to transmission spectroscopy observations (see Figure 17 and Table 10). The expected strength of the atmospheric signal is characterized by the transmission spectroscopy metric (TSM; Kempton et al. 2018), which is proportional to the host star's J

Table 7
Prior and Posterior Distributions of the Joint Transit RV Fit for Model $\mathcal{M}_{\rm lcp+GP}$ (Details in Section 4.3) Using Only the SPIRou Radial Velocities

Parameter	Prior[a]	Posterior	Description
		Fitted parameters	
$\rho_\star$ (g cm^{-3})	$\mathcal{N}(16.8, 1.9^2)$	$16.8^{+1.0}_{-1.4}$	Stellar density
P (days)	$\mathcal{U}(11.0, 11.1)$	11.06201 ± 0.00002	Orbital period
t_0 (BJD - 2 457 000)	$\mathcal{U}(1691.4, 1691.6)$	1691.5321 ± 0.0015	Time of inferior conjunction
r_1	$\mathcal{U}(0, 1)$	0.46 ± 0.08	Parameterization[b] for $R_{\rm p}/R_\star$ and b
r_2	$\mathcal{U}(0, 1)$	0.0555 ± 0.0014	Parameterization[b] for $R_{\rm p}/R_\star$ and b
K (m s^{-1})	$\mathcal{U}(0, 10)$	3.50 ± 0.94	RV semi-amplitude
e	0 (fixed)	0	Orbital eccentricity
ω (°)	90 (fixed)	90	Argument of periastron
$A_{\rm GP}$ (ms^{-1})	$\mathcal{LU}(10^{-2}, 100)$	$4.5^{+2.0}_{-1.2}$	Amplitude of the GP
$\ell_{\rm GP}$ (days)	$\mathcal{LU}(10^{-2}, 100)$	$11.3^{+12.0}_{-6.4}$	Timescale of the GP
$\gamma_{\rm SPIRou}$ (m s^{-1})	$\mathcal{U}(-33995, -33975)$	-33985 ± 2	SPIRou RV systemic component
$\sigma_{\rm SPIRou}$ (m s^{-1})	$\mathcal{U}(0, 10)$	2.3 ± 1.3	SPIRou RV extra white noise[c]
$q_{\rm 1,TESS}$	$\mathcal{U}(0, 1)$	$0.35^{+0.27}_{-0.19}$	TESS limb-darkening parameter[d]
$q_{\rm 2,TESS}$	$\mathcal{U}(0, 1)$	$0.37^{+0.33}_{-0.24}$	TESS limb-darkening parameter[d]
$D_{\rm TESS}$	1.0 (fixed)	1.0	TESS dilution factor
$M_{\rm TESS}$	$\mathcal{N}(0, 0.1^2)$	-0.00032 ± 0.00010	TESS baseline flux
$\sigma_{\rm TESS}$ (ppm)	$\mathcal{LU}(1, 10\,000)$	15^{+70}_{-12}	TESS extra white noise
$q_{\rm 1,PESTO}$	$\mathcal{U}(0, 1)$	$0.67^{+0.21}_{-0.26}$	PESTO limb-darkening parameter[d]
$q_{\rm 2,PESTO}$	$\mathcal{U}(0, 1)$	$0.46^{+0.28}_{-0.25}$	PESTO limb-darkening parameter[d]
$D_{\rm PESTO}$	$\mathcal{N}(0.564, 0.0564^2)$	0.586 ± 0.040	PESTO dilution factor
$M_{\rm PESTO}$	$\mathcal{N}(0, 0.1^2)$	0.00013 ± 0.00018	PESTO baseline flux
$\sigma_{\rm PESTO}$ (ppm)	$\mathcal{LU}(1, 10\,000)$	2287 ± 67	PESTO extra white noise
		$\vdots$	
		MuSCAT3 photometric parameters in Table 8	
		Derived parameters	
$R_{\rm p}$ ($R_\oplus$)	...	1.672 ± 0.071	Planetary radius
$M_{\rm p}$ ($M_\oplus$)	...	4.82 ± 1.30	Planetary mass
ρ (g cm^{-3})	...	$5.6^{+1.8}_{-1.6}$	Planetary bulk density
a (au)	...	0.061 ± 0.003	Orbital semimajor axis
$\delta \equiv (R_{\rm p}/R_\star)^2$	...	3.09 ± 0.16	Transit depth
b	...	0.19 ± 0.13	Transit impact parameter
i (°)	...	89.77 ± 0.16	Orbital inclination
$T_{\rm eq}$ (K)			Equilibrium temperature
$[A_{\rm B} = 0]$	...	326 ± 7	
$[A_{\rm B} = 0.3]$	...	298 ± 6	
$[A_{\rm B} = 0.77]$	...	226 ± 5	
S (S$_\oplus$)	...	1.8 ± 0.2	Insolation

Notes.
[a] $\mathcal{U}(a, b)$ is the uniform distribution between values a and b. $\mathcal{LU}(a, b)$ is the log-uniform (Jeffreys) distribution between values a and b. $\mathcal{N}(\mu, \sigma^2)$ is the normal distribution with mean μ and variance σ^2.
[b] Parameterization from Espinoza (2018).
[c] White noise term for single exposures within polarimetric sequences.
[d] $\{q_1, q_2\}$ are linked to the quadratic limb-darkening coefficients $\{u_1, u_2\}$ through the transformations outlined in Kipping (2013).

Table 8
Prior and Posterior Distributions of the MuSCAT3 Photometric Parameters for Model $\mathcal{M}_{\rm lcp+GP}$ (Details in Section 4.3) Using Only the SPIRou Radial Velocities

| Parameter	Prior	g'	r'	i'	$z_{\rm s}$
		Fitted parameters			
q_1	$\mathcal{U}(0, 1)$	$0.60^{+0.26}_{-0.31}$	$0.22^{+0.27}_{-0.15}$	$0.46^{+0.32}_{-0.27}$	$0.24^{+0.29}_{-0.16}$
q_2	$\mathcal{U}(0, 1)$	$0.59^{+0.27}_{-0.33}$	$0.37^{+0.35}_{-0.24}$	$0.24^{+0.28}_{-0.16}$	$0.27^{+0.33}_{-0.19}$
D	$\mathcal{U}(0.5, 1)$	0.71 ± 0.12	$0.88^{+0.07}_{-0.09}$	$0.96^{+0.03}_{-0.05}$	0.85 ± 0.07
M	$\mathcal{N}(0, 0.1^2)$	-0.00141 ± 0.00036	-0.00106 ± 0.00016	-0.00130 ± 0.00014	-0.00131 ± 0.00013
σ (ppm)	$\mathcal{LU}(1, 10\,000)$	2748 ± 319	46^{+427}_{-43}	1837^{+191}_{-206}	29^{+227}_{-26}
		Derived parameters			
$\delta_{\rm uncorr.}$ (ppt)	...	$2.18^{+0.40}_{-0.36}$	$2.72^{+0.21}_{-0.24}$	2.94 ± 0.17	2.64 ± 0.20
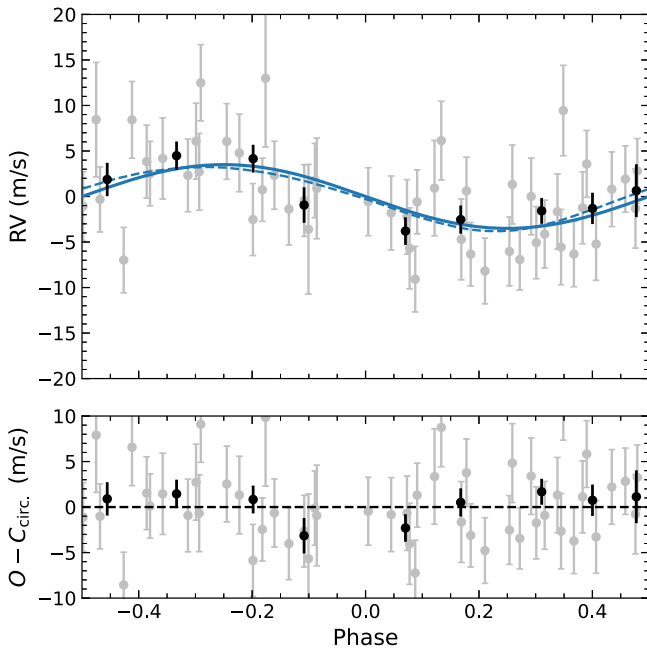
Figure 14. Phase-folded SPIRou RV curve, with systemic velocity and activity GP removed. Binned RV measurements (0.1 phase bin) are marked with black circles. The best-fit Keplerian models (blue) are depicted with a solid curve (circular orbit) and a dashed curve (eccentric orbit). The residuals of the circular fit are presented below. The circular solution yields smaller residuals rms (3.58 m s^{-1}) compared to the eccentric model (3.66 m s^{-1}); yet both Bayesian evidences are indistinguishable (see Figure 12).
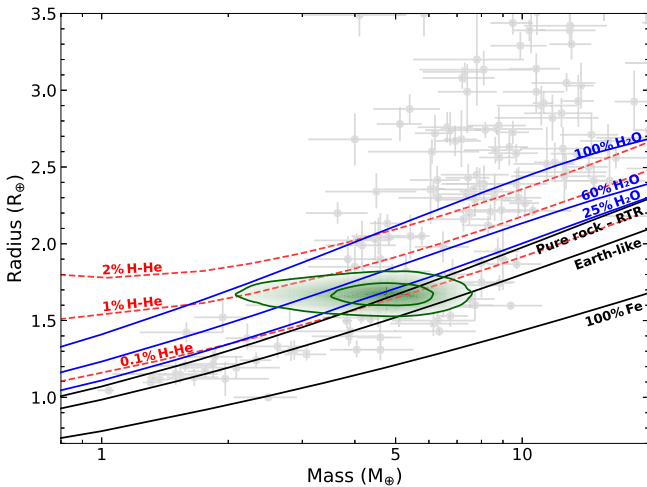
Figure 15. Mass–radius diagram of exoplanets (gray points). Only planets with mass and radius known with precision better than 30% are shown. Various theoretical composition curves are plotted, using interior structure models from Valencia et al. (2007), Valencia et al. (2013), Guillot & Morel (1995). All models assume no atmosphere, except the H–He (red dashed lines) models that correspond to Earth-like interior surrounded by a solar composition envelope at $T = 300$ K. The mass and radius posteriors (green 1 and 2σ contours) of TOI-1452b are consistent with either a water-rich interior with ~25% H_2O by mass, a pure rock (rocky threshold radius curve including relevant phase transitions), or a terrestrial planet with a thin hydrogen envelope of ~0.1% H–He by mass.

magnitude and the planet's atmospheric scale height. Figure 17 displays the TSM as a function of the equilibrium temperature for known small exoplanets with available mass measurements. The sample is restricted to systems with well-determined masses (relative uncertainty <30%) as a constraint on surface gravity is essential to correctly interpret the transmission spectrum of an exoplanet (Batalha et al. 2019). The temperate

subset of Figure 17 is detailed in Table 10. The TSM of TOI-1452b (39.9) is similar to well-known temperate systems such as LHS 1140b (50.0) and K2-18 b (40.8), while being 60% below the highest listed target in this subset, L231-32 d (TOI-270 d, 104.0). All seven host stars in Table 10 have $T_{\rm eff} < 4000$ K (or average $T_{\rm eff}$ of 3225 K), confirming the high interest of M dwarfs for planetary atmospheric characterization. Note that the high-value target L 98-59 d (TSM above 200; Cloutier et al. 2019; Demangeon et al. 2021) was just barely excluded from Table 10 due to its $T_{\rm eq}$ (409 K) being slightly above our 400 K cut. Our subset also excludes intriguing planets with plausible temperate environment but deprived of mass measurements (or imprecise mass), such as TOI-700 c (TSM = 79.7; Gilbert et al. 2020), TOI-1266c (TSM = 48.8; Demory et al. 2020) and K2-3 c (TSM = 25.5; Damasso et al. 2018). The TOI-1452 system is a unique target to explore the atmospheric properties of temperate planets within the radius valley. This paper provides the first mass determination needed for the interpretation of future transmission spectra.

5.3. Implications for the Emergence of the M Dwarf Radius Valley

Planets on either side of the radius valley differ by their composition, typically "rocky" for the smaller super-Earths, and "gaseous" for the larger mini-Neptunes. This transition occurs as a consequence of a varying envelope mass fraction: adding an H–He envelope up to a few percents of the total mass of a planet essentially doubles its observable radius (Lopez & Fortney 2014; Chen & Rogers 2016). Thermally driven atmospheric escape processes such as photoevaporation (Owen & Wu 2013; Lopez & Fortney 2014; Owen & Wu 2017; Lopez & Rice 2018; Wu 2019) and core-powered mass loss (Ginzburg et al. 2018; Gupta & Schlichting 2019, 2020) have been proposed as radius valley emergence mechanisms. In these models, super-Earths and mini-Neptunes originate from the same population of planets that form with an extended H–He envelope around an Earth-like core, with the population of rocky super-Earths emerging after losing their primordial atmospheres to hydrodynamic escape. Another possible scenario is to assemble rocky super-Earths at late times after most or all of the gas has been dissipated from the protoplanetary disk (Lee et al. 2014; Lopez & Rice 2018; Lee & Connors 2021). The two classes of planets would form on different timescales, resulting in a bimodal distribution without relying on any subsequent atmospheric escape.

Each of the aforementioned mechanisms predicts that the rocky-to-gaseous transition ($R_{\rm valley}$) varies with parameters such as the orbital period P and stellar mass $M_\star$. Photo-evaporation, core-powered mass-loss and gas-poor accretion models predict a negative slope in the $R_{\rm p}$–P space: $R_{\rm valley} \propto P^{-0.25 - 0.15}$ (Owen & Wu 2017; Lopez & Rice 2018; Mordasini 2020), $R_{\rm valley} \propto P^{-0.11}$ (Gupta & Schlichting 2019), and $R_{\rm valley} \propto P^{-0.08}$ (Lee & Connors 2021). Conversely, the formation of super-Earths strictly by the merging of planetary embryos in a gas-depleted environment, analogous to the formation of terrestrial planets in the solar system, would produce a positive slope ($R_{\rm valley} \propto P^{0.11}$; Lopez & Rice 2018). One way to test the proposed models is to compare these predictions to the real population of exoplanets.

From occurrence rate calculations of small close-in planets around Sun-like stars, Martinez et al. 2019 measured a $d \log R_{\rm valley}/d \log P = -0.11 \pm 0.02$, consistent with

Table 9
Chemical Ratios by Weight for the TOI-1452 System

Chemical Ratios	TOI-1452	Sun[a]	TOI-1452b No assumptions	TOI-1452b Stellar priors	TOI-1452b Bare rock
Fe/Mg	$1.48^{+0.36}_{-0.29}$	1.83 ± 0.25	$3.4^{+6.3}_{-2.2}$	$1.5^{+0.4}_{-0.4}$	$1.2^{+1.2}_{-0.6}$
Mg/Si	$0.86^{+0.37}_{-0.26}$	1.06 ± 0.13	0.86[b]	0.86[b]	0.86[b]
C/O	$0.48^{+0.11}_{-0.09}$	0.41 ± 0.07	[c]	[c]	[c]
CMF	...	...	$0.30^{+0.20}_{-0.17}$	$0.18^{+0.06}_{-0.06}$	$0.19^{+0.18}_{-0.12}$
WMF	...	...	$0.27^{+0.20}_{-0.15}$	$0.22^{+0.21}_{-0.13}$	...

Notes.
[a] Photospheric abundance ratios from Asplund et al. (2009).
[b] The Mg/Si ratios of the planets are fixed to the star TOI-1452 ratio.
[c] The interior models assume no carbon compounds.
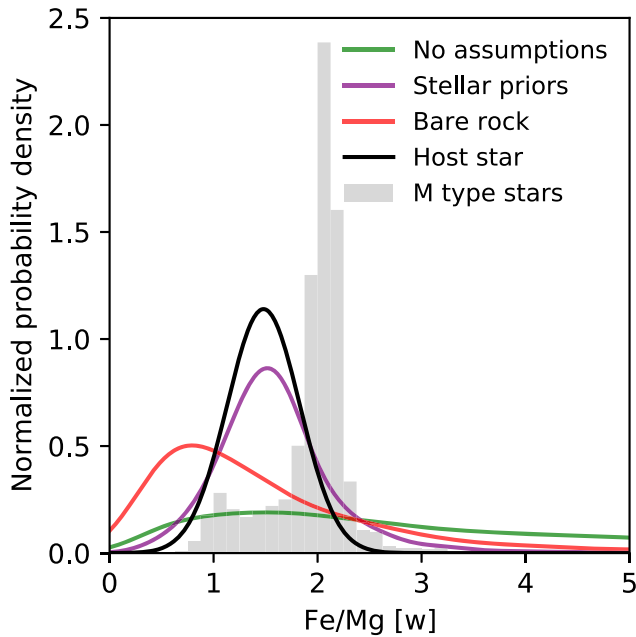
Figure 16. Fe/Mg distribution for TOI-1452b according to different model assumptions (Table 9) compared to that of its host star (black). We used kernel density estimate to draw the probabilities from the posteriors. We also include the M dwarfs distribution of Fe/Mg from the APOGEE database (gray histogram, sample size of ~1000; Majewski et al. 2016; Ahumada et al. 2020) for comparison.

thermally driven mass loss and gas-poor formation. Using a similar methodology but for planets around low-mass stars with $T_{\rm eff} < 4700$ K, Cloutier & Menou (2020) obtained a $d \log R_{\rm valley}/d \log P = 0.058 \pm 0.022$, where the positive sign suggests that the gas-depleted formation of super-Earths may be dominant around M dwarfs. These distinct slope measurements carve out regions in the $R_{\rm p}$–P parameter space where the models make opposing predictions regarding the bulk composition of a planet (i.e., either rocky or gaseous). This framework to test radius valley emergence models around M dwarfs was introduced in Cloutier & Menou (2020) and has since been applied to a number of transiting planets (TOIs 776 b, Luque et al. 2021; 1235b, Cloutier et al. 2020b; 1634b, Cloutier et al. 2021; 1685b, Bluhm et al. 2021).

Figure 18 presents the period–radius diagram for exoplanets around M-dwarf hosts ($T_{\rm eff} < 4000$ K). Each planet is color coded by its bulk density relative to the Earth-like structure model of Valencia et al. (2007; see Figure 15). TOI-1452b sits on or slightly above the empirical valley of Cloutier & Menou (2020), while being considerably below the slope measured by Martinez et al. (2019), scaled down to match the median stellar mass of the Cloutier & Menou (2020) sample (using Equation (11) therein). The locus of TOI-1452b in Figure 18, combined with our density estimate, are incompatible with the photo-evaporation and core-powered mass-loss models. However, the likely intermediate nature of TOI-1452b cannot strongly support the alternative gas-depleted formation scenario either as the dominant mechanism for the emergence of the M-dwarf radius valley. A volatile-rich interior for TOI-1452b could indicate a different formation pathway, e.g., one without significant gas accretion during the disk lifetime.

Figure 18 also highlights three other systems presenting similarities with TOI-1452b, namely, TOI-1235b (Cloutier et al. 2020b), L 98-59 d (Cloutier et al. 2019; Demangeon et al. 2021), and LHS 1140b (Dittmann et al. 2017; Lillo-Box et al. 2020). All four planets have a similar size, while spanning a large interval in periods. TOI-1235b ($P = 3.445$ days, $R_{\rm p} = 1.738\ R_\oplus$) and LHS 1140b ($P = 24.737$ days, $R_{\rm p} = 1.635\ R_\oplus$) have densities compatible with bona fide super-Earths; their position in Figure 18 indicates that they are probably examples of the largest terrestrial planets that can be assembled around M dwarfs without accreting a substantial hydrogen envelope. On the other hand, L 98-59 d ($P = 7.451$ days, $R_{\rm p} = 1.521\ R_\oplus$) is a likely water-rich (~30%) planet that may be approaching, like TOI-1452b, the minimum size for volatile-rich objects around a low-mass star. These four systems constitute benchmarks for understanding the formation and evolution of planets within the radius valley.

6. Summary & Conclusion

This paper reports the discovery and characterization of the transiting temperate exoplanet TOI-1452b. A joint analysis of transit observations from TESS and other ground-based telescopes combined with radial velocity measurements from SPIRou and IRD, yields a mass of $4.82 \pm 1.30\ M_\oplus$ and a radius of $1.672 \pm 0.071\ R_\oplus$. These physical parameters are consistent with either a rocky world with a Fe/Mg ratio similar to the host star (Fe/Mg $= 1.2^{+1.2}_{-0.6}$ by weight), a water-rich interior (either $22^{+21}_{-13}\%$ H_2O by weight, if stellar priors are assumed for the planetary refractory ratios, or $27^{+20}_{-15}\%$ H_2O if no assumptions are made) or a terrestrial planet surrounded by a $\lesssim 1\%$ H–He atmosphere. Orbiting its M4 host star ($T_{\rm eff} = 3185 \pm 50$ K) every 11.06201 ± 0.00002 days, the planet receives about twice as much radiation than the Earth ($S = 1.8 \pm 0.2\ S_\oplus$),

Table 10
TSM for a Subset of Well-characterized Small Exoplanets in a Temperate Equilibrium Temperature Regime (200 K ⩽ T_{eq} ⩽ 400 K)

Planet	P (days)	M_p ($M_\oplus$)	R_p ($R_\oplus$)	T_{eq} [$A_B = 0$] (K)	J (mag)	T_{eff} (K)	$M_\star$ ($M_\odot$)	$R_\star$ ($R_\odot$)	TSM	References
L231-32 d	11.380	4.78	2.133	388	9.10	3506	0.39	0.38	104.0	(1)
TOI-1231b	24.246	15.4	3.65	331	8.88	3553	0.48	0.48	97.6	(2)
LTT 3780c	12.252	8.6	2.30	353	9.01	3331	0.40	0.37	72.6	(3)
LHS 1140b	24.739	6.38	1.635	214	9.61	2988	0.19	0.21	50.0	(4)
K2-18 b	32.940	8.63	2.610	279	9.76	3457	0.50	0.44	40.8	(5)
TOI-1452b	11.062	4.82	1.672	326	10.60	3185	0.25	0.28	39.9	(6)
TRAPPIST-1 b	1.511	1.374	1.116	399	11.35	2566	0.09	0.12	28.6	(7)
TRAPPIST-1 d	4.049	0.388	0.788	287	11.35	2566	0.09	0.12	25.6	(7)
TRAPPIST-1 c	2.422	1.308	1.097	341	11.35	2566	0.09	0.12	24.3	(7)
TRAPPIST-1 e	6.101	0.692	0.920	251	11.35	2566	0.09	0.12	19.9	(7)
LHS 1140c	3.777	1.76	1.169	400	9.61	2988	0.19	0.21	18.7	(4)
TRAPPIST-1 f	9.208	1.039	1.045	218	11.35	2566	0.09	0.12	17.0	(7)

Note.
References: (1) Van Eylen et al. (2021). (2) Burt et al. (2021). (3) Cloutier et al. (2020a). (4) Lillo-Box et al. (2020). (5) Benneke et al. (2019). (6) This work. (7) Agol et al. (2021).
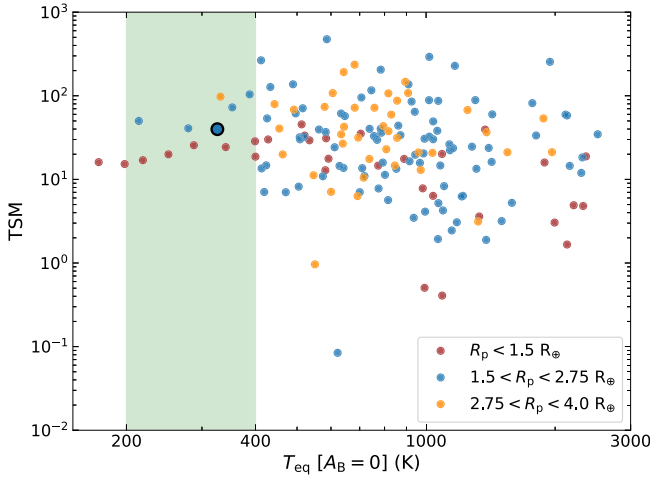
Figure 17. TSM (Kempton et al. 2018) as a function of the planetary equilibrium temperature for small exoplanets ($R_p < 4\,R_\oplus$) with well-established masses (error below 30%). The green region corresponds to an arbitrary temperate temperature interval (200 K ≤ T_{eq} ≤ 400 K). TOI-1452b is among the best temperate targets for follow-up transit spectroscopy with JWST.

corresponding to a blackbody temperature of 326 ± 7 K. The results of our interior modeling and the fact that the planet receives modest irradiation make TOI-1452b a good candidate water world.

TOI-1452b is a prime target for upcoming atmospheric characterization efforts with JWST, featuring a high transmission spectroscopy metric compared to other known temperate exoplanets. Transit spectroscopy observations with JWST should reveal the true nature of this intriguing exoplanet lying within the radius valley, whether this is a rocky world or one with a volatile envelope. Being observable with JWST most of the year, TOI-1452b is a unique system for studying exoplanets at the transition between super-Earths and mini-Neptunes.
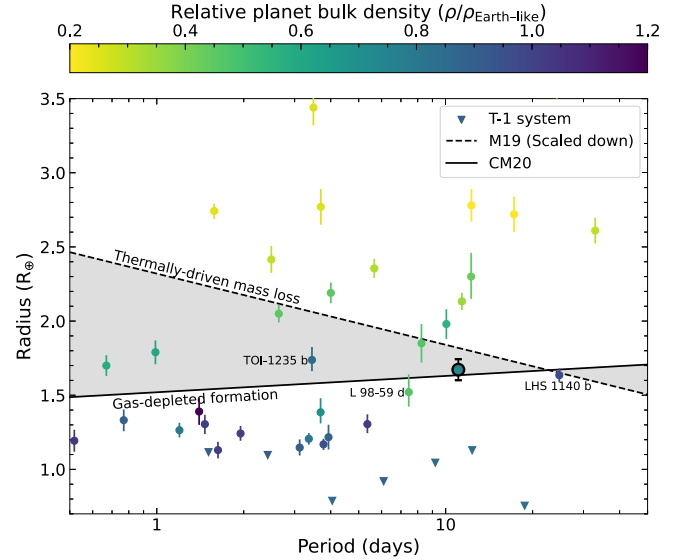
Figure 18. Period–radius diagram of exoplanets around low-mass stars ($T_{eff} \leqslant 4000$ K) with mass and radius known with precision better than 30%. The TRAPPIST-1 (T-1) planets are represented by triangles. Empirical *valleys* for low-mass stars from Cloutier & Menou 2020 (CM20), consistent with gas-depleted formation, and from Martinez et al. 2019 (M19), compatible with thermally driven atmospheric mass loss and scaled down to represent the stellar mass population of CM20. TOI-1452b lies below M19 and has a small bulk density compared to a terrestrial planet of the same mass ($\rho/\rho_{\rm Earth-like} \approx 0.76$). This is inconsistent with photoevaporation and core-powered mass-loss predictions.

Appendix A
TESS Light Curve

We present the TESS multisector PDCSAP light curve in Figure A1, with the exception of sectors 14 and 21, which were previously shown in Figure 2.
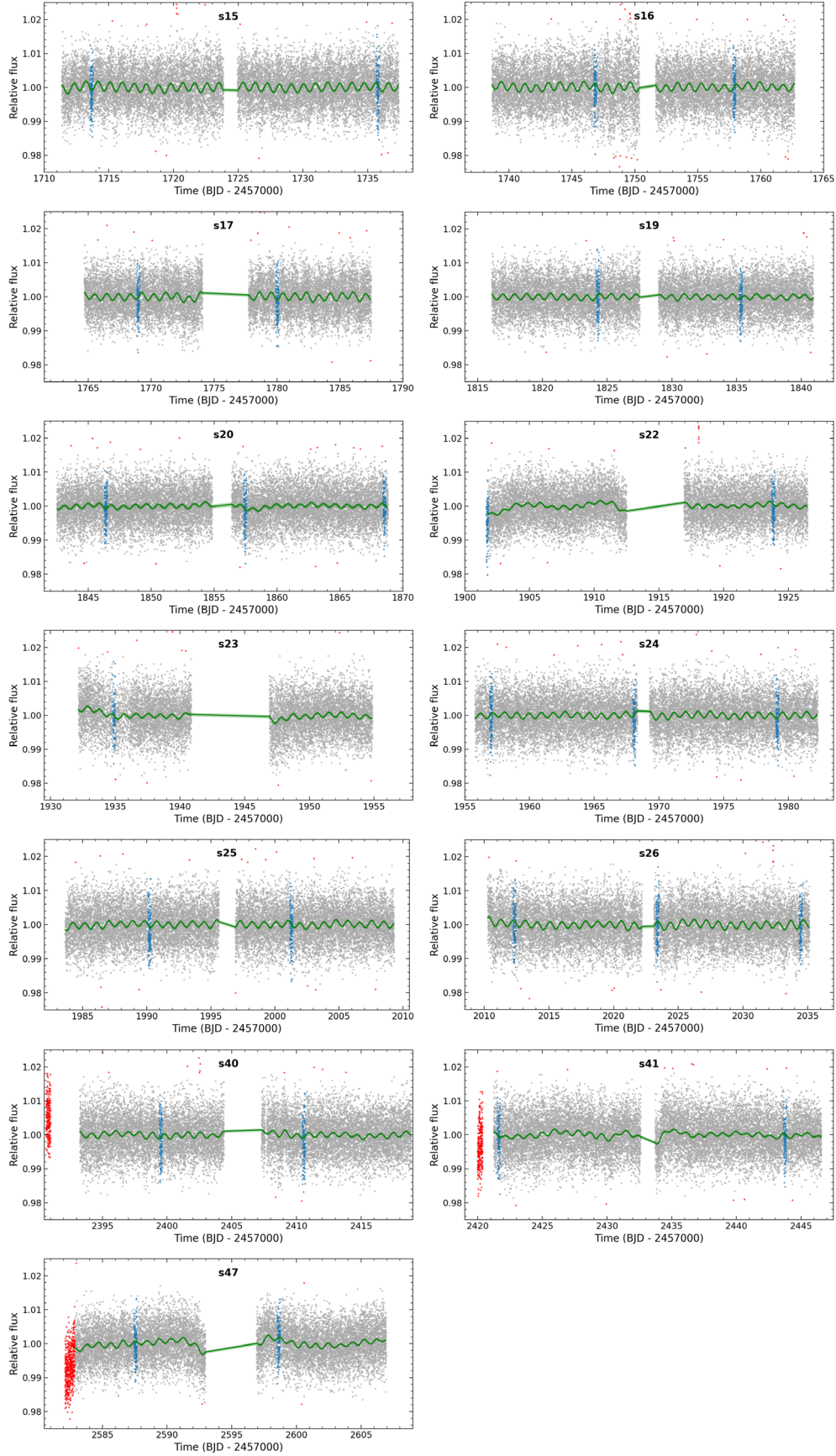
Figure A1. Normalized `PDCSAP` light curve of TOI-1452 from sectors 15–26 (except 18), 40–41, and 47. Sectors 14 and 21 were previously shown in Figure 2. The blue data points highlight the epochs of the detected transits, while the red data points are outliers/stellar flares rejected by sigma clipping (3.5 σ clip) or manually (in sectors 40, 41, or 47). The gaps in the light curve coincide with data downlink when TESS is close to perigee. The full light curve was modeled with a quasiperiodic Gaussian Process (green curve; details in Section 4.2).

Appendix B
Supplementary Material Regarding the Joint Transit RV Fit

In this appendix, we summarize the RV component of the joint transit RV models introduced in Section 4.3. The main RV parameters of the joint fits are reported in Table B1. All models and data sets detect TOI-1452b with a coherent semi-amplitude K. Models with an activity GP ($\mathcal{M}_{1cp+GP}$ and $\mathcal{M}_{1ep+GP}$) produced the highest Bayesian log-evidence (Figure 12) and needed the least extra white noise (σ_{SPIRou}, σ_{IRD}). We ultimately adopted the results of the SPIRou only joint fit because adding the seven IRD measurements yields similar Bayesian log-evidences and requires a σ_{IRD} about three times the level of the planetary signal (see Table B1).

Table B1
RV Component of the Joint Transit RV Fit for Different Models ($\mathcal{M}$) and Data Sets

Parameter	1cp	1cp+GP	1ep	1ep+GP
		SPIRou only		
K (m s^{-1})	4.2 ± 0.9	3.5 ± 0.9	4.7 ± 0.9	3.6 ± 0.9
e	$\cdots$	$\cdots$	0.20 ± 0.09	$0.12^{+0.12}_{-0.08}$
A_{GP} (m s^{-1})	$\cdots$	$4.5^{+2.0}_{-1.2}$	$\cdots$	$4.4^{+1.9}_{-1.2}$
ℓ_{GP} (days)	$\cdots$	$11.3^{+12.0}_{-6.4}$	$\cdots$	$11.6^{+12.4}_{-6.4}$
σ_{SPIRou} (m s^{-1})	4.9 ± 0.9	2.3 ± 1.3	$4.7^{+0.9}_{-1.0}$	2.2 ± 1.3
		SPIRou + IRD		
K (m s^{-1})	4.1 ± 0.9	3.5 ± 0.9	4.7 ± 0.9	3.6 ± 0.9
e	$\cdots$	$\cdots$	0.19 ± 0.09	$0.12^{+0.12}_{-0.08}$
A_{GP} (m s^{-1})	$\cdots$	$4.7^{+2.3}_{-1.3}$	$\cdots$	$4.6^{+2.2}_{-1.2}$
ℓ_{GP} (days)	$\cdots$	$11.1^{+11.2}_{-6.2}$	$\cdots$	$11.7^{+11.2}_{-6.2}$
σ_{SPIRou} (ms^{-1})	4.9 ± 0.9	2.3 ± 1.3	$4.7^{+0.9}_{-1.0}$	$2.3^{+1.2}_{-1.3}$
σ_{IRD} (m s^{-1})	$13.6^{+5.4}_{-3.6}$	$11.5^{+5.7}_{-4.3}$	$14.2^{+5.7}_{-3.8}$	$11.9^{+5.5}_{-4.1}$

Notes. $\mathcal{M}_{1cp}$: single circular orbit planet. $\mathcal{M}_{1cp+GP}$: single circular orbit planet and activity GP. $\mathcal{M}_{1ep}$: single eccentric orbit planet. $\mathcal{M}_{1ep+GP}$: single eccentric orbit planet and activity GP.

Appendix C
Summary of Interior Parameters

We present in this appendix the corner plots from the MCMC modeling of the planetary interior. Figures C1 and C2 summarize the cases when water is allowed to be significant in the interior, respectively, when no assumptions on the refractory ratios (Fe/Si and Mg/Si) are made and when the planet follows the refractory ratios of its host star. Figure C3 presents the result of the bare rock scenario.
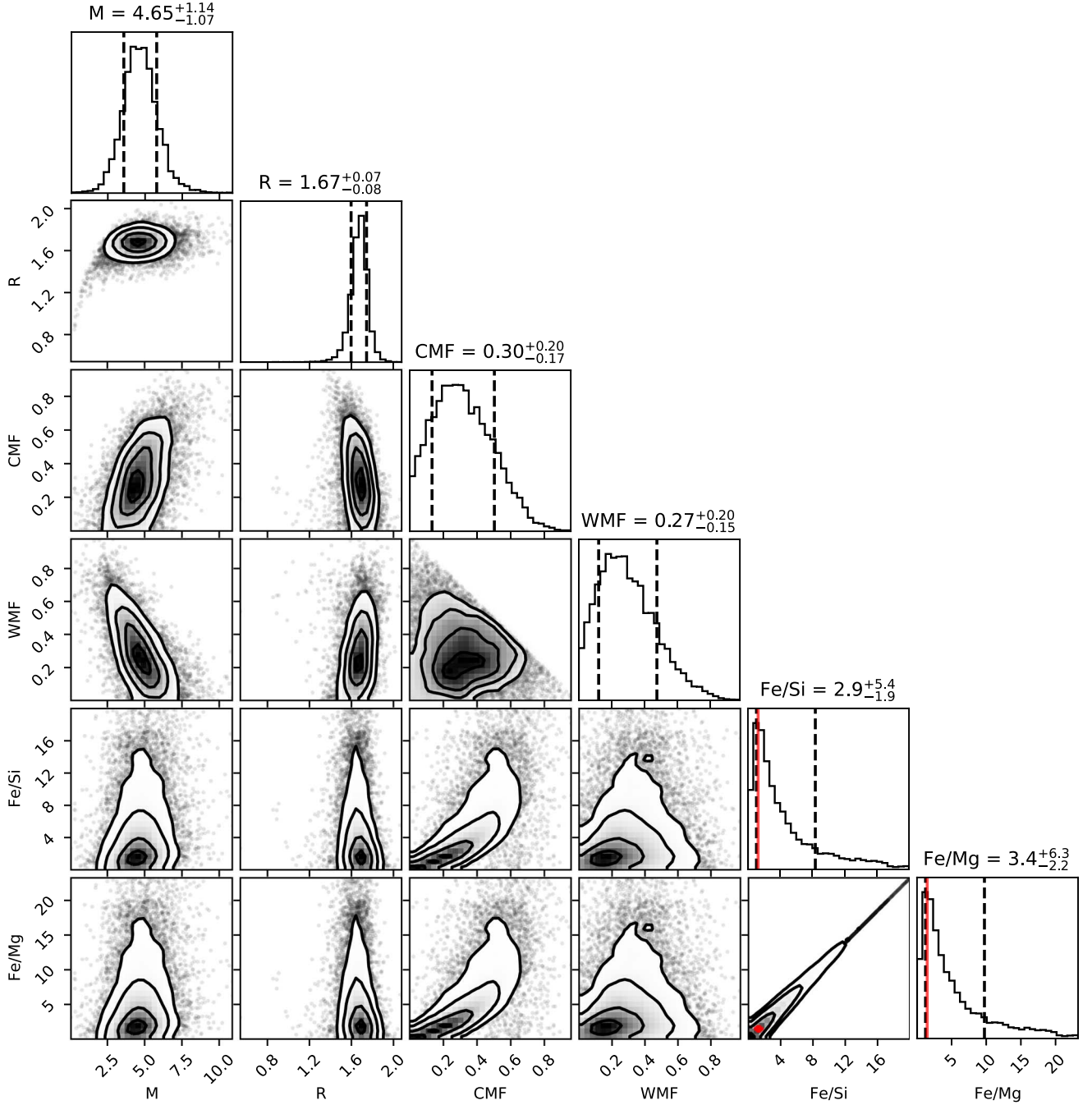

Figure C1. No assumptions, corner plot summary for TOI-1452b interior parameters where the core-mass fraction (CMF) and water-mass fraction (WMF) are simulated quantities for a given planetary mass and radius. Chemical ratios Fe/Si and Mg/Si are derived quantities. The vertical red lines in the Fe/Si, Fe/Mg space are the mean stellar refractory ratios, and the vertical dashed lines represent 16th and 84th percentiles.
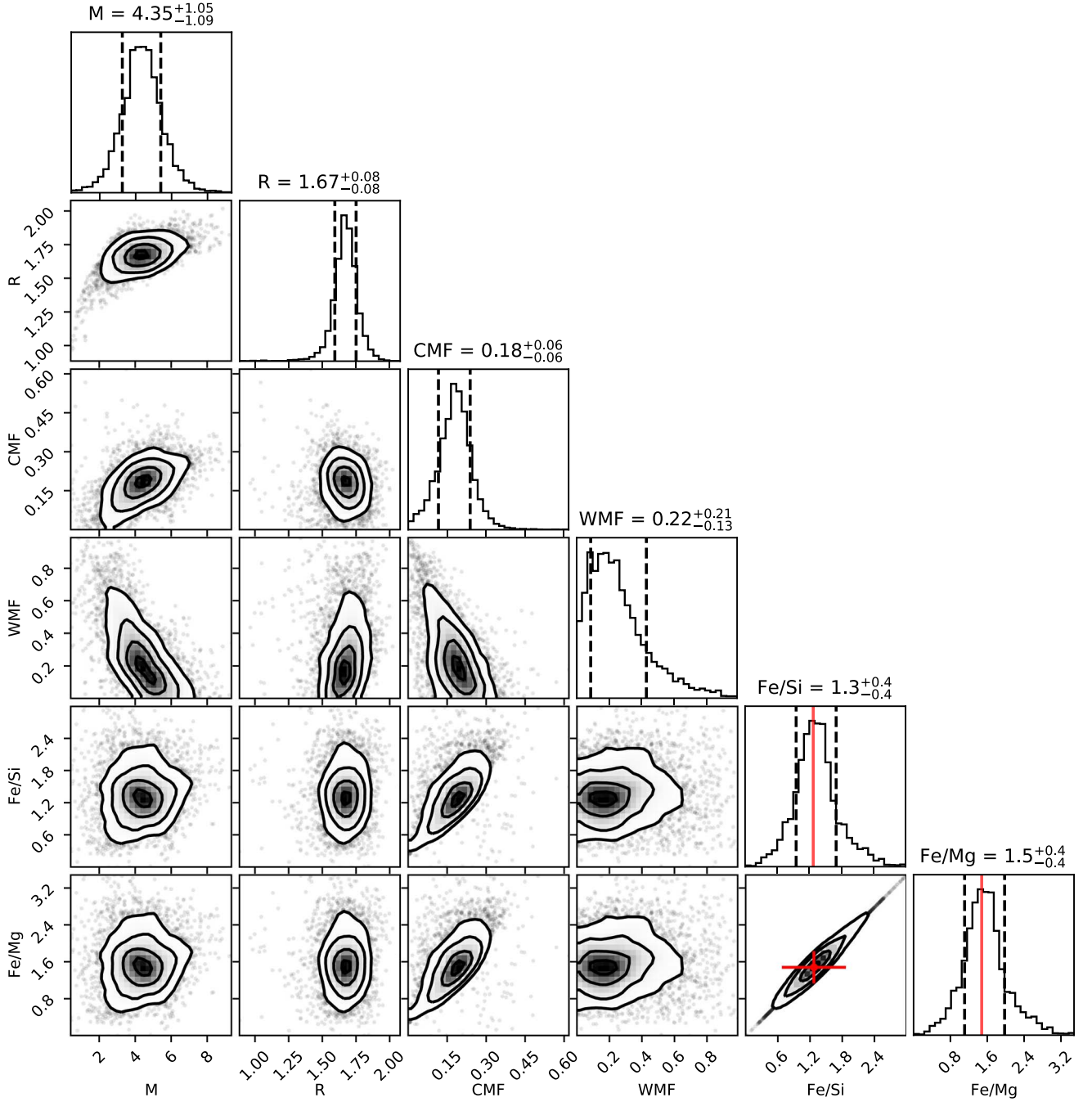
Figure C2. Stellar prior, corner plot summary for TOI-1452b interior parameters where we assume that the planet follows stellar refractory ratios for a given planetary mass and radius. Thus, the log-probability function is modified to include the restriction posed by the Fe/Mg ratio of the star and can be written as Fe/Mg $\sim \mathcal{N}(\mathrm{Fe_*/Mg_*}, \sigma_{\mathrm{Fe_*/Mg_*}})$. The red and dashed vertical lines represent the stellar ratios and 16th and 84th percentiles of the posterior, respectively.
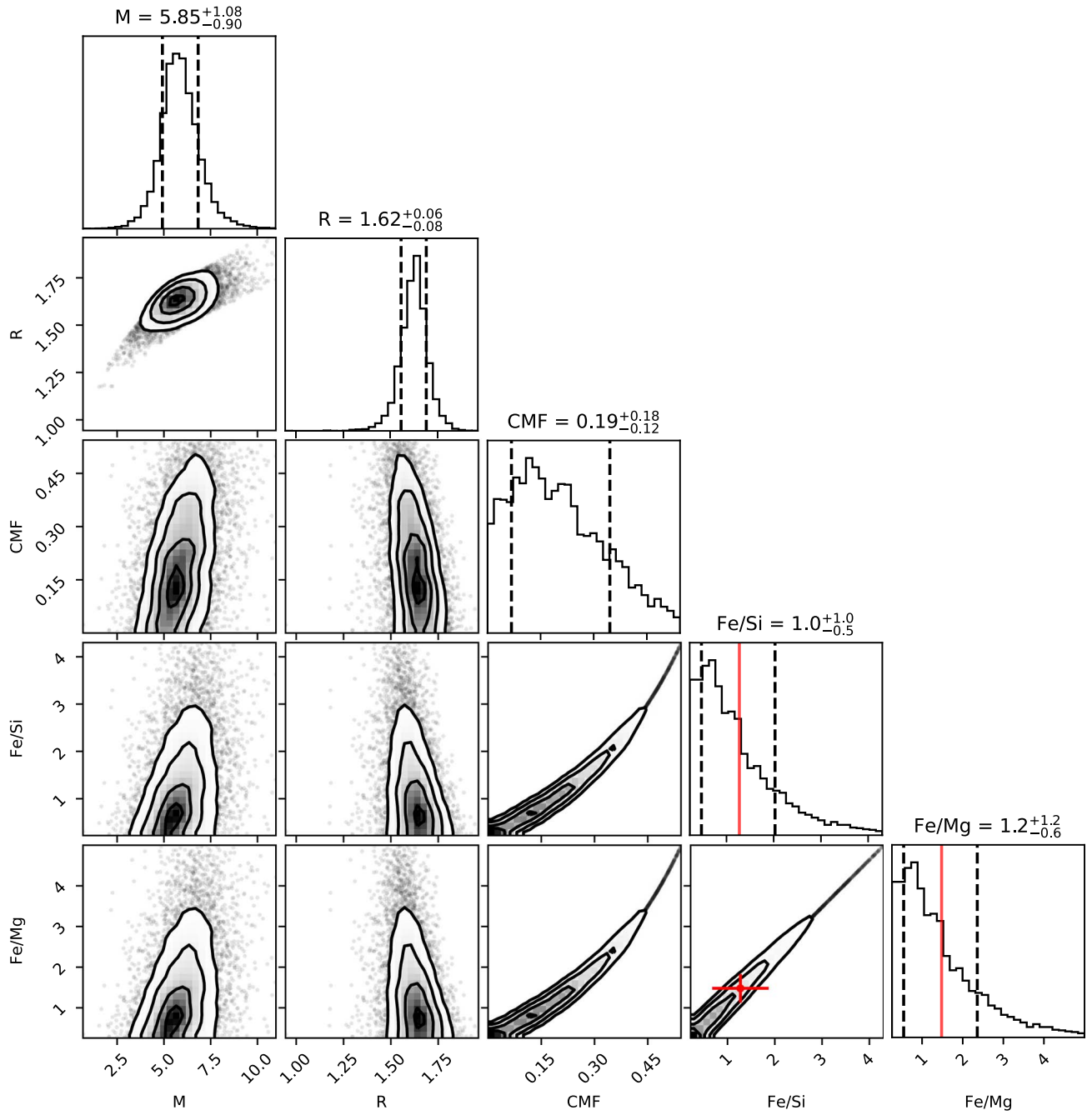
Figure C3. Bare rock, corner plot summary for TOI-1452b interior parameters where we assume only rocky composition is possible (no water) for a given planetary mass and radius. Chemical ratios Fe/Si and Mg/Si are derived quantities. The red and dashed vertical lines represent the stellar ratios and 16th and 84th percentiles of the posterior, respectively.

Appendix D
Radial Velocity Measurements

We present the radial velocity measurements of TOI-1452 from SPIRou and IRD in the online Table D1.

Table D1
SPIRou and IRD RV Measurements

Instrument	BJD - 2 400 000	RV (m s^{-1})	σ_{RV} (m s^{-1})
SPIRou	59004.995291	−33983.32	8.39
SPIRou	59005.006067	−33975.16	8.12
SPIRou	59005.016836	−33980.21	8.25
SPIRou	59005.027551	−33995.65	8.28
SPIRou	59009.008115	−33975.18	8.02
SPIRou	59009.018950	−33974.66	8.20
SPIRou	59009.029725	−33975.25	7.96
…	…	…	…
IRD	59118.766592	15.17	4.08
IRD	59122.769496	17.14	3.86
IRD	59122.787278	14.54	3.77
IRD	59156.837456	−14.4	4.86
IRD	59372.001844	−9.95	3.71
IRD	59373.904952	2.00	5.70
IRD	59390.850628	12.31	4.03

Note. Table D1 is published in its entirety in the machine-readable format. A portion is shown here for guidance regarding its form and content.

(This table is available in its entirety in machine-readable form.)

ORCID iDs

Charles Cadieux ⓘ https://orcid.org/0000-0001-9291-5555
René Doyon ⓘ https://orcid.org/0000-0001-5485-4675
Mykhaylo Plotnykov ⓘ https://orcid.org/0000-0002-9479-2744
Guillaume Hébrard ⓘ https://orcid.org/0000-0001-5450-7067
Farbod Jahandar ⓘ https://orcid.org/0000-0003-0029-2835
Étienne Artigau ⓘ https://orcid.org/0000-0003-3506-5667
Diana Valencia ⓘ https://orcid.org/0000-0003-3993-4030
Neil J. Cook ⓘ https://orcid.org/0000-0003-4166-4121
Eder Martioli ⓘ https://orcid.org/0000-0002-5084-168X
Thomas Vandal ⓘ https://orcid.org/0000-0002-5922-8267
Jean-François Donati ⓘ https://orcid.org/0000-0001-5541-2887
Ryan Cloutier ⓘ https://orcid.org/0000-0001-5383-9393
Norio Narita ⓘ https://orcid.org/0000-0001-8511-2981
Akihiko Fukui ⓘ https://orcid.org/0000-0002-4909-5763
Teruyuki Hirano ⓘ https://orcid.org/0000-0003-3618-7535
François Bouchy ⓘ https://orcid.org/0000-0002-7613-393X
Nicolas B. Cowan ⓘ https://orcid.org/0000-0001-6129-5699
Erica J. Gonzales ⓘ https://orcid.org/0000-0002-9329-2190
David R. Ciardi ⓘ https://orcid.org/0000-0002-5741-3047
Keivan G. Stassun ⓘ https://orcid.org/0000-0002-3481-9052
Luc Arnold ⓘ https://orcid.org/0000-0002-0111-1234
Björn Benneke ⓘ https://orcid.org/0000-0001-5578-1498
Isabelle Boisse ⓘ https://orcid.org/0000-0002-1024-9841
Xavier Bonfils ⓘ https://orcid.org/0000-0001-9003-8894
Andrés Carmona ⓘ https://orcid.org/0000-0003-2471-1299
Pía Cortés-Zuleta ⓘ https://orcid.org/0000-0002-6174-4666
Xavier Delfosse ⓘ https://orcid.org/0000-0001-5099-7978
Thierry Forveille ⓘ https://orcid.org/0000-0003-0536-4607
Pascal Fouqué ⓘ https://orcid.org/0000-0002-1436-7351
João Gomes da Silva ⓘ https://orcid.org/0000-0001-8056-9202
Jon M. Jenkins ⓘ https://orcid.org/0000-0002-4715-9460
Flavien Kiefer ⓘ https://orcid.org/0000-0001-9129-4929
Ágnes Kóspál ⓘ https://orcid.org/0000-0001-7157-6275
David Lafrenière ⓘ https://orcid.org/0000-0002-6780-4252
Jorge H. C. Martins ⓘ https://orcid.org/0000-0002-1532-9082
Claire Moutou ⓘ https://orcid.org/0000-0002-2842-3924
J.-D. do Nascimento, Jr. ⓘ https://orcid.org/0000-0001-7804-2145
Stefan Pelletier ⓘ https://orcid.org/0000-0002-8573-805X
Joseph D. Twicken ⓘ https://orcid.org/0000-0002-6778-7552
Luke G. Bouma ⓘ https://orcid.org/0000-0002-0514-5538
Antoine Darveau-Bernier ⓘ https://orcid.org/0000-0002-7786-0661
Konstantin Grankin ⓘ https://orcid.org/0000-0001-5707-8448
Masahiro Ikoma ⓘ https://orcid.org/0000-0002-5658-5971
Taiki Kagetani ⓘ https://orcid.org/0000-0002-5331-6637
Kiyoe Kawauchi ⓘ https://orcid.org/0000-0003-1205-5108
Takanori Kodama ⓘ https://orcid.org/0000-0001-9032-5826
Takayuki Kotani ⓘ https://orcid.org/0000-0001-6181-3142
David W. Latham ⓘ https://orcid.org/0000-0001-9911-7388
George Ricker ⓘ https://orcid.org/0000-0003-2058-6662
Sara Seager ⓘ https://orcid.org/0000-0002-6892-6948
Motohide Tamura ⓘ https://orcid.org/0000-0002-6510-0681
Roland Vanderspek ⓘ https://orcid.org/0000-0001-6763-6562
Noriharu Watanabe ⓘ https://orcid.org/0000-0002-7522-8195

References

Agol, E., Dorn, C., Grimm, S. L., et al. 2021, PSJ, 2, 1
Ahumada, R., Prieto, C. A., Almeida, A., et al. 2020, ApJS, 249, 3
Akeson, R. L., Chen, X., Ciardi, D., et al. 2013, PASP, 125, 989
Allard, F., Homeier, D., & Freytag, B. 2012a, RSPTA, 370, 2765
Allard, F., Homeier, D., Freytag, B., Schaffenberger, W., & Rajpurohit, A. S. 2013, MSAIS, 24, 128
Allard, F., Homeier, D., Freytag, B., & Sharp, C. M. 2012b, in Low-Mass Stars and the Transition Stars/Brown Dwarfs - EES2011 (EAS Publications Series, Vol. 57) ed. C. Reylé, C. Charbonne, & M. Schultheis (Les Ulis: EDP), 3
Artigau, E., Saint-Antoine, J., Lévesque, P.-L., et al. 2018, Proc. SPIE, 10709, 107091P
Artigau, É., Astudillo-Defru, N., Delfosse, X., et al. 2014, Proc. SPIE, 9149, 914905
Artigau, É., Hébrard, G., Cadieux, C., et al. 2021, AJ, 162, 144
Artigau, E., Cadieux, C., Cook, N. J., et al. 2022, arXiv:2207.13524
Asplund, M., Grevesse, N., Sauval, A. J., & Scott, P. 2009, ARA&A, 47, 481
Astropy Collaboration, Price-Whelan, A. M., Sipőcz, B. M., et al. 2018, AJ, 156, 123
Barnes, R., & Heller, R. 2013, AsBio, 13, 279
Batalha, N. E., Lewis, T., Fortney, J. J., et al. 2019, ApJL, 885, L25
Bean, J. L., Stevenson, K. B., Batalha, N. M., et al. 2018, PASP, 130, 114402
Benneke, B., Wong, I., Piaulet, C., et al. 2019, ApJL, 887, L14
Berger, T. A., Huber, D., Gaidos, E., van Saders, J. L., & Weiss, L. M. 2020, AJ, 160, 108
Bertaux, J. L., Lallement, R., Ferron, S., Boonne, C., & Bodichon, R. 2014, A&A, 564, A46
Bluhm, P., Pallé, E., Molaverdikhani, K., et al. 2021, A&A, 650, A78
Bolmont, E., Selsis, F., Owen, J. E., et al. 2017, MNRAS, 464, 3728
Boucher, A., Darveau-Bernier, A., Pelletier, S., et al. 2021, AJ, 162, 233
Bouchy, F., Pepe, F., & Queloz, D. 2001, A&A, 374, 733
Bradley, L., Sipőcz, B., Robitaille, T., et al. 2020, astropy/photutils: 1.0.0, Zenodo, doi:10.5281/zenodo.4044744
Burt, J. A., Dragomir, D., Mollière, P., et al. 2021, AJ, 162, 87
Chabrier, G. 2001, ApJ, 554, 1274
Chambers, K. C., Magnier, E. A., Metcalfe, N., et al. 2016, arXiv:1612.05560
Chen, H., & Rogers, L. A. 2016, ApJ, 831, 180
Cloutier, R., & Menou, K. 2020, AJ, 159, 211
Cloutier, R., Astudillo-Defru, N., Bonfils, X., et al. 2019, A&A, 629, A111
Cloutier, R., Eastman, J. D., Rodriguez, J. E., et al. 2020a, AJ, 160, 3

Cloutier, R., Rodriguez, J. E., Irwin, J., et al. 2020b, AJ, 160, 22
Cloutier, R., Charbonneau, D., Stassun, K. G., et al. 2021, AJ, 162, 79
Collins, K. A., Kielkopf, J. F., Stassun, K. G., & Hessman, F. V. 2017, AJ, 153, 77
Courcol, B., Bouchy, F., Pepe, F., et al. 2015, A&A, 581, A38
Crossfield, I. J. M., Waalkes, W., Newton, E. R., et al. 2019, ApJL, 883, L16
Cushing, M. C., Rayner, J. T., & Vacca, W. D. 2005, ApJ, 623, 1115
Damasso, M., Bonomo, A. S., Astudillo-Defru, N., et al. 2018, A&A, 615, A69
David, T. J., Contardo, G., Sandoval, A., et al. 2021, AJ, 161, 265
Demangeon, O. D. S., Zapatero Osorio, M. R., Alibert, Y., et al. 2021, A&A, 653, A41
Demory, B. O., Pozuelos, F. J., Gómez Maqueo Chew, Y., et al. 2020, A&A, 642, A49
Dittmann, J. A., Irwin, J. M., Charbonneau, D., et al. 2017, Natur, 544, 333
Donati, J. F., Semel, M., Carter, B. D., Rees, D. E., & Collier Cameron, A. 1997, MNRAS, 291, 658
Donati, J.-F., Kouach, D., Lacombe, M., et al. 2018, in SPIRou: A NIR Spectropolarimeter/High-Precision Velocimeter for the CFHT, ed. H. J. Deeg & J. A. Belmonte (Cham: Springer), 107
Donati, J. F., Kouach, D., Moutou, C., et al. 2020, MNRAS, 498, 5684
Dreizler, S., Crossfield, I. J. M., Kossakowski, D., et al. 2020, A&A, 644, A127
Dressing, C. D., & Charbonneau, D. 2015, ApJ, 807, 45
El-Badry, K., Rix, H.-W., & Heintz, T. M. 2021, MNRAS, 506, 2269
Espinoza, N. 2018, RNAAS, 2, 209
Espinoza, N., Kossakowski, D., & Brahm, R. 2019, MNRAS, 490, 2262
Foreman-Mackey, D. 2018, RNAAS, 2, 31
Foreman-Mackey, D., Agol, E., Ambikasaran, S., & Angus, R. 2017, AJ, 154, 220
Foreman-Mackey, D., Hogg, D. W., Lang, D., & Goodman, J. 2013, PASP, 125, 306
Foreman-Mackey, D., Farr, W., Sinha, M., et al. 2019, JOSS, 4, 1864
Fressin, F., Torres, G., Charbonneau, D., et al. 2013, ApJ, 766, 81
Fukui, A., Narita, N., Tristram, P. J., et al. 2011, PASJ, 63, 287
Fulton, B. J., & Petigura, E. A. 2018, AJ, 156, 264
Fulton, B. J., Petigura, E. A., Blunt, S., & Sinukoff, E. 2018, PASP, 130, 044504
Fulton, B. J., Petigura, E. A., Howard, A. W., et al. 2017, AJ, 154, 109
Gagné, J., Mamajek, E. E., Malo, L., et al. 2018, ApJ, 856, 23
Gaia Collaboration, Brown, A. G. A., Vallenari, A., et al. 2021, A&A, 649, A1
Gilbert, E. A., Barclay, T., Schlieder, J. E., et al. 2020, AJ, 160, 116
Ginzburg, S., Schlichting, H. E., & Sari, R. 2018, MNRAS, 476, 759
Girardi, L., Barbieri, M., Groenewegen, M. A. T., et al. 2012, ApSSP, 26, 165
Guerrero, N. M., Seager, S., Huang, C. X., et al. 2021, ApJS, 254, 39
Guillot, T., & Morel, P. 1995, A&AS, 109, 109
Günther, M. N., Pozuelos, F. J., Dittmann, J. A., et al. 2019, NatAs, 3, 1099
Gupta, A., & Schlichting, H. E. 2019, MNRAS, 487, 24
Gupta, A., & Schlichting, H. E. 2020, MNRAS, 493, 792
Gustafsson, B., Edvardsson, B., Eriksson, K., et al. 2008, A&A, 486, 951
Hardegree-Ullman, K. K., Zink, J. K., Christiansen, J. L., et al. 2020, ApJS, 247, 28
Harris, C. R., Millman, K. J., van der Walt, S. J., et al. 2020, Natur, 585, 357
Hauschildt, P. H., Allard, F., & Baron, E. 1999, ApJ, 512, 377
Hemley, R. J., Jephcoat, A. P., Mao, H. K., et al. 1987, Natur, 330, 737
Higson, E., Handley, W., Hobson, M., & Lasenby, A. 2019, Statist. Comput., 29, 891
Hirano, T., Kuzuhara, M., Kotani, T., et al. 2020, PASJ, 72, 93
Hobson, M. J., Bouchy, F., Cook, N. J., et al. 2021, A&A, 648, A48
Horne, K. 1986, PASP, 98, 609
Howard, A. W., Marcy, G. W., Johnson, J. A., et al. 2010, Sci, 330, 653
Howard, A. W., Marcy, G. W., Bryson, S. T., et al. 2012, ApJS, 201, 15
Hunter, J. D. 2007, CSE, 9, 90
Husser, T. O., Wende-von Berg, S., Dreizler, S., et al. 2013, A&A, 553, A6
Jenkins, J. M. 2002, ApJ, 575, 493
Jenkins, J. M., Tenenbaum, P., Seader, S., et al. 2020, in Kepler Science Document KSCI-19081-003, ed. J. M. Jenkins (Moffett Field, CA: Kepler Project Office)
Jenkins, J. M., Chandrasekaran, H., McCauliff, S. D., et al. 2010, Proc. SPIE, 7740, 77400D
Jenkins, J. M., Twicken, J. D., McCauliff, S., et al. 2016, Proc. SPIE, 9913, 99133E
Jensen, E. 2013, Tapir: A web interface for transit/eclipse observability, Astrophysics Source Code Library, ascl:1306.007
Kempton, E. M. R., Bean, J. L., Louie, D. R., et al. 2018, PASP, 130, 114401

Kiman, R., Schmidt, S. J., Angus, R., et al. 2019, AJ, 157, 231
Kipping, D. M. 2013, MNRAS, 435, 2152
Kotani, T., Tamura, M., Nishikawa, J., et al. 2018, Proc. SPIE, 10702, 1070211
Kramida, A., Ralchenko, Y., Reader, J. & NIST ASD Team 2021, NIST Atomic Spectra Database (v5.9)
Kreidberg, L. 2015, PASP, 127, 1161
Lee, E. J., Chiang, E., & Ormel, C. W. 2014, ApJ, 797, 95
Lee, E. J., & Connors, N. J. 2021, ApJ, 908, 32
Li, J., Tenenbaum, P., Twicken, J. D., et al. 2019, PASP, 131, 024506
Lillo-Box, J., Barrado, D., & Bouy, H. 2014, A&A, 566, A103
Lillo-Box, J., Figueira, P., Leleu, A., et al. 2020, A&A, 642, A121
Lopez, E. D., & Fortney, J. J. 2014, ApJ, 792, 1
Lopez, E. D., & Rice, K. 2018, MNRAS, 479, 5303
Luque, R., Serrano, L. M., Molaverdikhani, K., et al. 2021, A&A, 645, A41
Majewski, S. R. & APOGEE Team 2016, AN, 337, 863
Mann, A. W., Feiden, G. A., Gaidos, E., Boyajian, T., & von Braun, K. 2015, ApJ, 804, 64
Mann, A. W., Gaidos, E., & Ansdell, M. 2013, ApJ, 779, 188
Mann, A. W., Dupuy, T., Kraus, A. L., et al. 2019, ApJ, 871, 63
Martinez, C. F., Cunha, K., Ghezzi, L., & Smith, V. V. 2019, ApJ, 875, 29
Martioli, E., Hébrard, G., Moutou, C., et al. 2020, A&A, 641, L1
Martioli, E., Hébrard, G., Fouqué, P., et al. 2022, A&A, 660, A86
Mayo, A. W., Vanderburg, A., Latham, D. W., et al. 2018, AJ, 155, 136
McCully, C., Turner, M., Volgenau, N., et al. 2018, LCOGT/banzai: Initial Release, 0.9.4, Zenodo, doi:10.5281/zenodo.1257560
McDonald, G. D., Kreidberg, L., & Lopez, E. 2019, ApJ, 876, 22
McQuillan, A., Aigrain, S., & Mazeh, T. 2013, MNRAS, 432, 1203
Micheau, Y., Challita, Z., Gallou, G., et al. 2018, Proc. SPIE, 10702, 107025R
Mordasini, C. 2020, A&A, 638, A52
Moutou, C., Dalal, S., Donati, J. F., et al. 2020, A&A, 642, A72
Mugrauer, M., & Michel, K.-U. 2020, AN, 341, 996
Muirhead, P. S., Dressing, C. D., Mann, A. W., et al. 2018, AJ, 155, 180
Narita, N., Fukui, A., Yamamuro, T., et al. 2020, Proc. SPIE, 11447, 114475K
Newton, E. R., Mondrik, N., Irwin, J., Winters, J. G., & Charbonneau, D. 2018, AJ, 156, 217
Owen, J. E., & Murray-Clay, R. 2018, MNRAS, 480, 2206
Owen, J. E., & Wu, Y. 2013, ApJ, 775, 105
Owen, J. E., & Wu, Y. 2017, ApJ, 847, 29
Pecaut, M. J., & Mamajek, E. E. 2013, ApJS, 208, 9
Petigura, E. A., Marcy, G. W., Winn, J. N., et al. 2018, AJ, 155, 89
Piskunov, N. E., Kupka, F., Ryabchikova, T. A., Weiss, W. W., & Jeffery, C. S. 1995, A&AS, 112, 525
Plotnykov, A., & Valencia, D. 2020, MNRAS, 499, 932
Rayner, J. T., Cushing, M. C., & Vacca, W. D. 2009, ApJS, 185, 289
Reylé, C., Jardine, K., Fouqué, P., et al. 2021, A&A, 650, A201
Ricker, G. R., Winn, J. N., Vanderspek, R., et al. 2015, JATIS, 1, 014003
Rogers, J. G., Gupta, A., Owen, J. E., & Schlichting, H. E. 2021, MNRAS, 508, 5886
Scora, J., Valencia, D., Morbidelli, A., & Jacobson, S. 2020, MNRAS, 493, 4910
Skilling, J. 2006, BayAn, 1, 833
Skrutskie, M. F., Cutri, R. M., Stiening, R., et al. 2006, AJ, 131, 1163
Smith, J. C., Stumpe, M. C., Van Cleve, J. E., et al. 2012, PASP, 124, 1000
Sokal, A. 1997, in Monte Carlo Methods in Statistical Mechanics: Foundations and New Algorithms, ed. C. DeWitt-Morette, P. Cartier, & A. Folacci (Boston, MA: Springer), 131
Speagle, J. S. 2020, MNRAS, 493, 3132
Stassun, K. G., Collins, K. A., & Gaudi, B. S. 2017, AJ, 153, 136
Stassun, K. G., Corsaro, E., Pepper, J. A., & Gaudi, B. S. 2018a, AJ, 155, 22
Stassun, K. G., & Torres, G. 2016, AJ, 152, 180
Stassun, K. G., & Torres, G. 2021, ApJL, 907, L33
Stassun, K. G., Oelkers, R. J., Pepper, J., et al. 2018b, AJ, 156, 102
Stassun, K. G., Oelkers, R. J., Paegert, M., et al. 2019, AJ, 158, 138
Stetson, P. B. 1987, PASP, 99, 191
Stewart, S. T., & Ahrens, T. J. 2005, JGRE, 110, E03005
Stumpe, M. C., Smith, J. C., Catanzarite, J. H., et al. 2014, PASP, 126, 100
Stumpe, M. C., Smith, J. C., Van Cleve, J. E., et al. 2012, PASP, 124, 985
Sullivan, P. W., Winn, J. N., Berta-Thompson, Z. K., et al. 2015, ApJ, 809, 77
Tamura, M., Suto, H., Nishikawa, J., et al. 2012, Proc. SPIE, 8446, 84461T
Trotta, R. 2008, ConPh, 49, 71
Twicken, J. D., Catanzarite, J. H., Clarke, B. D., et al. 2018, PASP, 130, 064502
Valencia, D., Guillot, T., Parmentier, V., & Freedman, R. S. 2013, ApJ, 775, 10

Valencia, D., Sasselov, D. D., & O'Connell, R. J. 2007, ApJ, 656, 545
Van Eylen, V., Agentoft, C., Lundkvist, M. S., et al. 2018, MNRAS, 479, 4786
Van Eylen, V., Astudillo-Defru, N., Bonfils, X., et al. 2021, MNRAS, 507, 2154
Virtanen, P., Gommers, R., Oliphant, T. E., et al. 2020, NatMe, 17, 261

Winters, J. G., Medina, A. A., Irwin, J. M., et al. 2019, AJ, 158, 152
Wright, E. L., Eisenhardt, P. R. M., Mainzer, A. K., et al. 2010, AJ, 140, 1868
Wu, Y. 2019, ApJ, 874, 91
Zacharias, N., Finch, C. T., Girard, T. M., et al. 2013, AJ, 145, 44
Zechmeister, M., Reiners, A., Amado, P. J., et al. 2018, A&A, 609, A12